J. Fluid Mech. (1980), *vol.* 100, *part* 3, *pp.* 471–511
Printed in Great Britain

The impingement of underexpanded, axisymmetric jets on perpendicular and inclined flat plates

By P. J. LAMONT† AND B. L. HUNT‡

Department of Aeronautical Engineering,
University of Bristol, England

(Received 18 June 1979)

This paper reports on an extensive experimental study of the flows due to underexpanded axisymmetric jets impinging on flat plates. The range of plate locations extends to a point where the jet is just subsonic but the main emphasis is on the behaviour in the first shock cell. Plate inclinations from 90° to 30° were investigated by means of comprehensive surface pressure measurements and shadowgraph pictures. Wherever possible, the main features of the results have been reconstructed using inviscid analyses of the wave interactions.

The flows are shown to be extremely complex due to the local structure of the free jet and, particularly, due to interactions between shock waves in the free jet and those created by the plate. In the near field, these interactions tend to be the controlling factors but at larger distances from the nozzle, mixing effects become increasingly important.

The maximum pressure on the plate when it is inclined can be very much larger than when the plate is perpendicular, owing to the possibility of high pressure recoveries through multiple shock systems. Correlations are presented for some of the main features on perpendicular plates and it is shown that the integrated pressure loads for both normal and inclined plates can be predicted well by a simple momentum balance.

1. Introduction

Problems created by the impingement of supersonic jets on solid objects arise in a wide variety of situations among which the authors are aware of the following: multi-stage rocket separation, deep-space docking, space-module attitude-control thruster operation, lunar and planetary landing and take-off, jet-engine exhaust impingement, gas-turbine blade failure, gun-muzzle blast impingement, shock-impingement heating and terrestrial rocket launch. These impingement flows are generally found to be extremely complex. They contain mixed subsonic and supersonic regions, elaborate interacting shock and expansion systems, highly non-uniform upstream flows (in the form of the free jet), regions of turbulent shear and instances of major flow instabilities. In the case of rocket motors, high temperatures and solid particles must be added to this already formidable list. Not surprisingly, it is often still necessary to conduct *ad*

† Present address: Department of Fluid Mechanics, University of Manchester, England.
‡ Present address: Northrop Corporation, 3901 West Broadway, Hawthorne, California, U.S.A.

0022-1120/80/4482-2170 $02.00

hoc tests on specific configurations when practical information is required. Nonetheless, a background of understanding is gradually being developed by means of systematic laboratory studies using simple shapes. This paper reports an investigation in which the impingement is on perpendicular and inclined flat plates and the jets are of air at the moderate pressure ratios found in terrestrial launch applications.

Previous work in this area has concentrated on perpendicular plates. One of the first applications to attract interest was that of impingement in deep space and this gave rise to a number of studies using a near-vacuum environment; a fairly recent example is the report by Clark (1970). Results obtained under these conditions are only of very limited relevance to impingment in an atmosphere because the shock interactions which are important at moderate pressure ratios occur in regions of low density and are relatively unimportant in deep space. Studies using perpendicular flat plates at atmospheric conditions have been carried out by many workers, of whom examples are Ginzburg *et al.* (1968), Gummer & Hunt (1974), Ginzburg *et al.* (1970), Gubanova, Lunev & Plastinina (1974) and Kalghatgi & Hunt (1976). The last three papers are principally concerned with the phenomenon of stagnation bubbles which will also be encountered later in this paper. This rather curious flow consists of a closed bubble of recirculating air which extends over the central region of the plate under the main plate shock.

In contrast to the fairly large number of investigations involving perpendicular plates, there have been only two relevant studies of impingement on inclined plates. These are due to Henderson (1966) and to Donaldson & Snedeker (1971). Henderson's work was done with uniform jets of Mach numbers 1·8, 2·01 and 2·14. The plate inclinations ranged from 20° to 90°. The relevance of Henderson's work to the present paper is only very limited because of the simplicity of his jets; furthermore, Henderson's surface pressure tappings were rather widely spaced with consequent lack of definition in the pressure distributions. Of all the previous work, the study conducted by Donaldson & Snedeker (1971) (see also Snedeker & Donaldson 1964, 1965) is the most closely related to that reported here. Donaldson & Snedeker used air from a sonic orifice operated at underexpansion ratios of 1·42 and 3·57, the plate was inclined to the jet within the angular range 15° to 90° and was mainly located at four positions down the axis, two of which were within the subsonic far field. The principal impingement data which were collected were plate pressures in the plane of symmetry and along a line perpendicular to it, and schlieren pictures for the perpendicular plate. Donaldson & Snedeker's main concern was with the influence of turbulent mixing and they therefore also conducted an extensive and careful study of the turbulence and mean velocities in the free jet. At the larger plate distances, Donaldson & Snedeker managed to correlate successfully a number of quantities from the impingement flow fields with their measured free-jet characteristics; however, their treatments break down in the near jet where the shock structure, rather than turbulent mixing, has the dominant effect.

This paper is concerned principally with impingement in the near field, where there is at present very little information. Underexpanded, cold air jets were produced by a supersonic nozzle representative of certain rocket motors. Surface pressure distributions covering the entire impingement region and corresponding shadowgraph pictures were obtained. In this paper, most attention is given to cases where the plate is inclined to the axis but the results for a perpendicular plate are also discussed. The

main emphasis is on identifying and understanding the most important features of the flow.

The material presented here is only a selection from an extensive set. Limited numbers of copies of the complete data are available in report form from the authors (Lamont & Hunt 1977).

2. Experimental apparatus

Compressed air for the jets was supplied to the nozzles by rig II of Carling & Hunt's (1974) work. This is connected to a 30 bar main and incorporates a control valve and a settling chamber. The pressure in the chamber is displayed on a Budenberg test gauge. Early on in the work, it was found that acoustic reflexion from the base of the settling chamber produced unsteadiness in the impingement flows under some conditions (see § 5 for details). The base of the chamber was then covered with a thick layer of cotton padding, which acted as a sound absorber.

Two nozzles were used; both are of the convergent–divergent type with an identical design downstream of the throat. This consists of an initial expansion in the form of a circular arc with radius equal to the throat diameter, which is 21·4 mm, and a conical exit section of 15° semi-angle. The exit diameter, D_N, is 30 mm, giving a design lip Mach number of 2·2. One of the nozzles, referred to here as the 'short nozzle', is that used previously by Lamont & Hunt (1976); it has an entry contraction whose final section is a circular arc of radius equal to 2·56 times the throat diameter. The other nozzle, referred to as the 'long nozzle', has an elliptical entry contour whose radius of curvature at the throat is 5·2 times the throat diameter. The long nozzle was used for small and moderate plate spacings ($z_{NP} < 5D_N$ where z_{NP} is the distance measured along the axis from the nozzle outlet plane to the plate) while the short nozzle was used for tests at $z_{NP} = 7$, 10 and 15 diameters. The long nozzle was made in order to prevent the plate from fouling the acoustic damping material on the rig at the smaller angles of inclination. The nozzles were operated at underexpansion ratios, PR, of 1·2 and 2 where PR is defined to be the ratio of the static pressure at the lip of the nozzle to the ambient pressure.

The plate used is a circular disk of diameter 300 mm (ten times the nozzle exit diameter). It contains forty-seven pressure tappings arranged along a diameter. Over an inner radial distance of 60 mm, the holes are spaced 3 mm apart (the outer holes are spaced more widely) but because the arrangement is asymmetric about the central hole, the resolution can be doubled if necessary by revolving the plate through an angle of 180°. A complete footprint of pressures can be obtained by setting the pressure tapped diameter at a series of azimuthal angles. The standard values used were 0, 30°, 60° and 90°, where the datum is the plane of symmetry; additional angles were used where greater resolution was required. The plate was mounted on a traversing rig which enabled the pressure holes to be centred.

The pressures were measured with a 35 bar Druck strain-gauge transducer mounted in a Scanivalve unit. At each port, three samples were taken of the electrical output; these were digitized, recorded on paper tape and subsequently processed on a Hewlett Packard 2100A computer.

A focused shadowgraph system was used to obtain photographs of the flow field. It employed a conventional single-pass arrangement with a continuous light source.

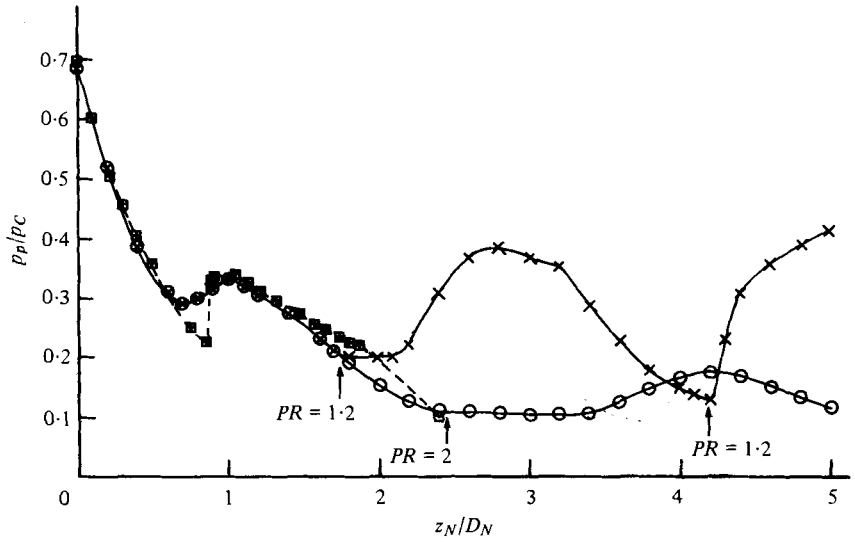

FIGURE 1. Distribution of pitot pressures along the jet axis. —×—, measured, $PR = 1{\cdot}2$; —○—, measured, $PR = 2$; – – + – –, computed, $PR = 1{\cdot}2$; – – ⊞ – –, computed, $PR = 2$; ↑, location of free jet Mach disk from shadowgraph.

3. The free jets

Information on the structure and properties of the free jets was obtained in a variety of ways and will be presented in this section. The main emphasis was on the near regions of the jets ($z_N \lesssim 5D_N$).

The most detailed information was obtained from a non-homentropic method of characteristics program (Prozan 1966; Butler 1966) which will be referred to here as the 'Lockheed plume program'. Starting data were given just downstream of the nozzle throat and were calculated by the method of Sauer (1947). When the inward-running characteristics intersect as the jet shock wave forms, the Lockheed plume program inserts the exact Rankine–Hugoniot relations. The calculation breaks down at an axial location near where the first Mach disk is found to lie in practice; upstream of this station, it gives complete information on the flow field. The accuracy of the predicted values will be considered shortly.

The overall wave structure in the jets was determined, as far as possible, from shadowgraph pictures. In each case, the shadowgraphs were obtained in sections along the jet and a composite was then constructed from the sectional pictures. The shadowgraphs of the first shock cell and part of the second were quite clear but the structure further downstream was blurred by turbulent mixing; there was nothing to be seen at distances greater than 10 diameters from the nozzle exit. From a study of the shadowgraphs, Mach disks or shock crossings were identified on the centre-line of the $PR = 1{\cdot}2$ jet at the following axial distances, expressed in nozzle exit diameters, 1·78, 4·2, 6·8 and 9·6. For the $PR = 2$ jet, the corresponding distances were 2·44, 5·5 and 9·9. The jet shock location near the nozzle was found to agree very well with that predicted by the Lockheed plume program.

Pitot measurements were made along part of the axes of the jets from the long nozzle: the results are presented in figure 1, where the locations of the Mach disks, as

seen on the shadowgraphs, are also shown and a comparison is made with values predicted by the Lockheed plume program. The main features of these distributions are as follows. The pitot pressure initially falls as axial distance, z_N, increases because the Mach number rises owing initially to the radial nature of the flow leaving the nozzle and subsequently to the expansion waves originating on the nozzle lip. The recompression region at $z_N \cong 0{\cdot}85$ diameters, is due to a weak shock wave (called here the nozzle shock) which is a consequence of overexpansion in the nozzle on the high curvature section just downstream of the throat (Lamont & Hunt 1976; Back & Cuffel 1966). The pitot pressure remains constant in the flow immediately downstream of the Mach disk, which is subsonic and inviscid. It then rises owing to the inward diffusion of air of high total pressure from the outer part of the jet. The pitot pressure starts to fall again when the centre flow becomes supersonic and additional shock losses occur. The agreement between the predicted and measured pitot pressures is seen to be very good. There is some discrepancy in the detail of the nozzle shock but this may well be due either to interference between the probe and the shock wave or to small differences between the manufactured contour of the nozzle and that which was prescribed to the program.

Radial distributions of pitot reading were also obtained at axial distances from the nozzle of 0·75, 1·5, 5, 7, 10 and 15 diameters. Again, the agreement between the measured and predicted pressures in the near jet was very good.

A comparison of pitot pressures measured in the jets from the long and the short nozzles shows a slight discrepancy in the location of the nozzle shock (presumably due to small differences in the wall contours) but elsewhere the results agree well.

4. Reliability

Care was taken to check the reliability of the results. This was done by three methods: by repeating a number of the tests, by conducting tests at small plate spacings with the short nozzle for comparison with the results from the long nozzle and by taking measurements with a sonic orifice of underexpansion ratio 3·57, for comparison with Donaldson & Snedeker's (1971) results at $z_{NP} = 1{\cdot}96D_N$ and at $z_{NP} = 7{\cdot}32D_N$. Consistency was excellent except under certain conditions to be discussed below. An example of the good agreement obtained with Donaldson & Snedeker's results is shown in figure 2 which applies for a plate angle of 60° and a location, z_{NP}, of $1{\cdot}96D_N$. Donaldson & Snedeker were mainly concerned with effects near the axis and it can be seen from this figure that their pressure distribution does not extend far enough to cover the very large pressure peak contained in our results. The implications of this will be discussed in § 7.

Discrepancies in the high pressure region were found in a few cases in all of which the plate was perpendicular to the jet axis and located in the supersonic part of the second shock cell; stagnation bubbles existed in every case. Most of these flows were not subject to any major unsteadiness. The discrepancies thus seem to be due to the high sensitivity of the bubble flow to small differences in the jet structure, these differences presumably originate either in small differences in the nozzles or in differing mixing rates produced by differing turbulence levels. In one case, problems of acoustically induced unsteadiness had to be eliminated (see § 5) and it is possible that some of the discrepancies may originate in acoustic feedback phenomena. Finally, it should

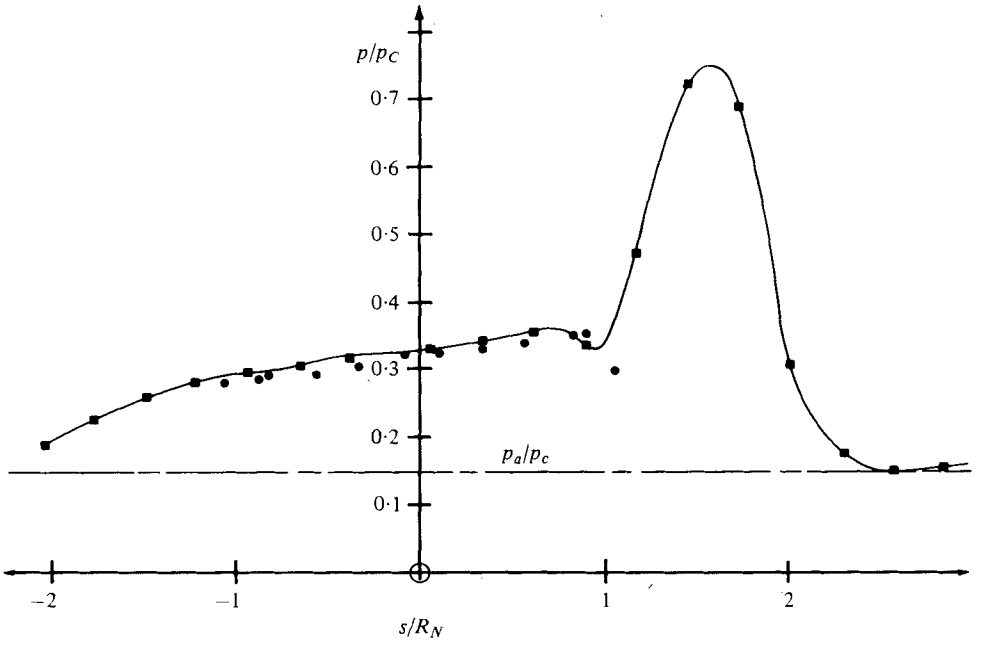

FIGURE 2. Surface pressures on the plane of symmetry for a sonic orifice with $PR = 3{\cdot}57$, $z_{NP} = 1{\cdot}96D_N$, $\theta = 60°$. ■, current results; ●, Snedeker & Donaldson (1965).

be noted that the discrepancies occurred in only a very few cases, that they existed mainly at the pressure peaks and that they did not exceed 15 %.

5. Unsteadiness

Unsteadiness of the flow has quite frequently been reported in supersonic jet impingement studies and was encountered occasionally in the present work. It normally manifests itself in motion of the shock wave, which consequently appears blurred on continuous light source photographs, and in fluctuations of the plate pressures. There appear to be three possible causes of flow unsteadiness although they are not well understood. A low frequency (1–10 Hz) variation is sometimes encountered when a stagnation bubble repeatedly forms and disperses (Gubanova *et al.* 1974; Kalghatgi & Hunt 1976); this did not occur in the present tests. Higher frequency unsteadiness can apparently be induced by acoustic standing waves set up between the plate and any parallel surface in the vicinity of the nozzle (Nakatogawa, Hirat & Kukita 1974). Finally, large pressure fluctuations with frequencies in the range 14–20 kHz can be produced, probably by Hartmann resonance in which travelling shock waves reflect between the oscillating plate shock and the plate (Back & Sarohia 1978; Henderson 1966).

In the tests described here, no evidence of unsteadiness was present in the sampled pressures; this is not surprising in view of the long lengths (1·5 m) of pressure tubing. However, there were occasions when the shock waves were blurred and appeared to be unsteady. The first such occasion arose when a sonic orifice was being used for comparison with the results of Donaldson & Snedeker (1971). The particular conditions of the test were a perpendicular plate with $z_{NP} = 7{\cdot}32D_N$ and $PR = 3{\cdot}57$. The problem

was solved by covering the rather large (300 mm diameter) base of the reservoir from which the nozzle protruded with sound absorbing material, suggesting that acoustic standing waves were the cause. Further details and a photograph may be found in the report by Lamont & Hunt (1977).

In the main set of tests with the Mach 2·2 nozzle, there was some evidence of unsteadiness at $PR = 1{\cdot}2$ for $z_{NP} = 1{\cdot}5D_N$ on a perpendicular plate but not at other locations. When the pressure ratio was 2 and the plate perpendicular, the shadowgraphs for $z_{NP} = 2D_N$, $2{\cdot}44D_N$ and $3D_N$ all show evidence of considerable unsteadiness of the plate shock, although not of the jet itself. Smaller scale disturbances can be seen in the same jet at $z_{NP} = 1{\cdot}5D_N$ and $z_{NP} = 4D_N$. In all cases, the unsteadiness was found to decrease rapidly with plate inclination, θ, and by $\theta = 70°$ was no longer detectable at any plate location.

It seems most likely that the cause of the unsteadiness in the above cases was the Hartmann generator mechanism in view of the success of the sound absorbing material in eliminating the standing waves for the sonic orifice and in view of the observation that the jet shocks did not seem to be affected. It was also found that the observed conditions of instability agreed fairly well with those recorded by Semiletenko & Uskov (1972) with a similar (but not identical) nozzle.

It is evident that the question of unsteadiness needs investigating but it was not within the scope of the present study to do so. If it is indeed a phenomenon which is inherent to the flow, rather than being dependent on the experimental rig, then the pressures presented here for the cases where it occurred will be meaningful time averaged values. The number of cases involved is in any case small.

6. The perpendicular plate

The results in the form of pressure distributions and selected shadowgraphs are discussed in § 6.1 and some empirical correlations of important aspects of the flow are presented in § 6.2.

6.1. *Discussion of results*

The measured pressure distributions are presented in figure 3 and some shadowgraphs may be found in figure 4 (plates 1 and 2). For clarity, the experimental points have been omitted from the distributions with the exception of the two curves at seven diameters. From these cases it can be seen that good resolution was achieved. The plate location is denoted by z_{NP}, its distance from the exit plane of the nozzle measured in nozzle exit diameters. The pressures are normalised with respect to p_C, the pressure in the supply chamber. Distance s is measured from the jet axis; R_N denotes nozzle exit radius.

It can be seen that, as the plate is moved away from the nozzle, the pressure distributions and shock structures for the two underexpansion ratios follow similar sequences. Close to the nozzle the pressure distribution is smooth, with a maximum value on the centre-line; the shape is similar to that found for accurately uniform jets (Gummer & Hunt 1971). The region of rapid expansion between $s/R_N \cong 1$ and $s/R_N \cong 2$ is produced by the expansion fan which exists at the intersection of the plate shock with the jet edge. The subsequent alternating compression and expansion regions in the wall jet are produced by the repeated reflexions of the waves from the

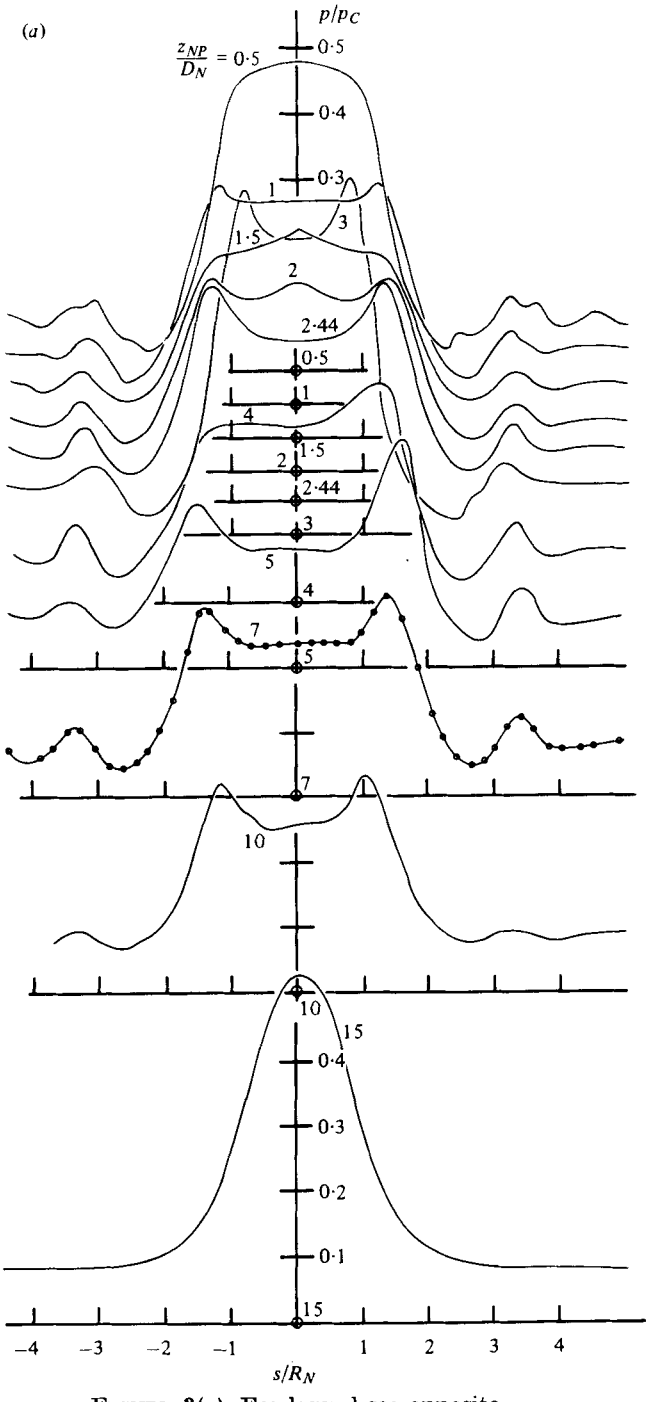

FIGURE 3(*a*). For legend see opposite.

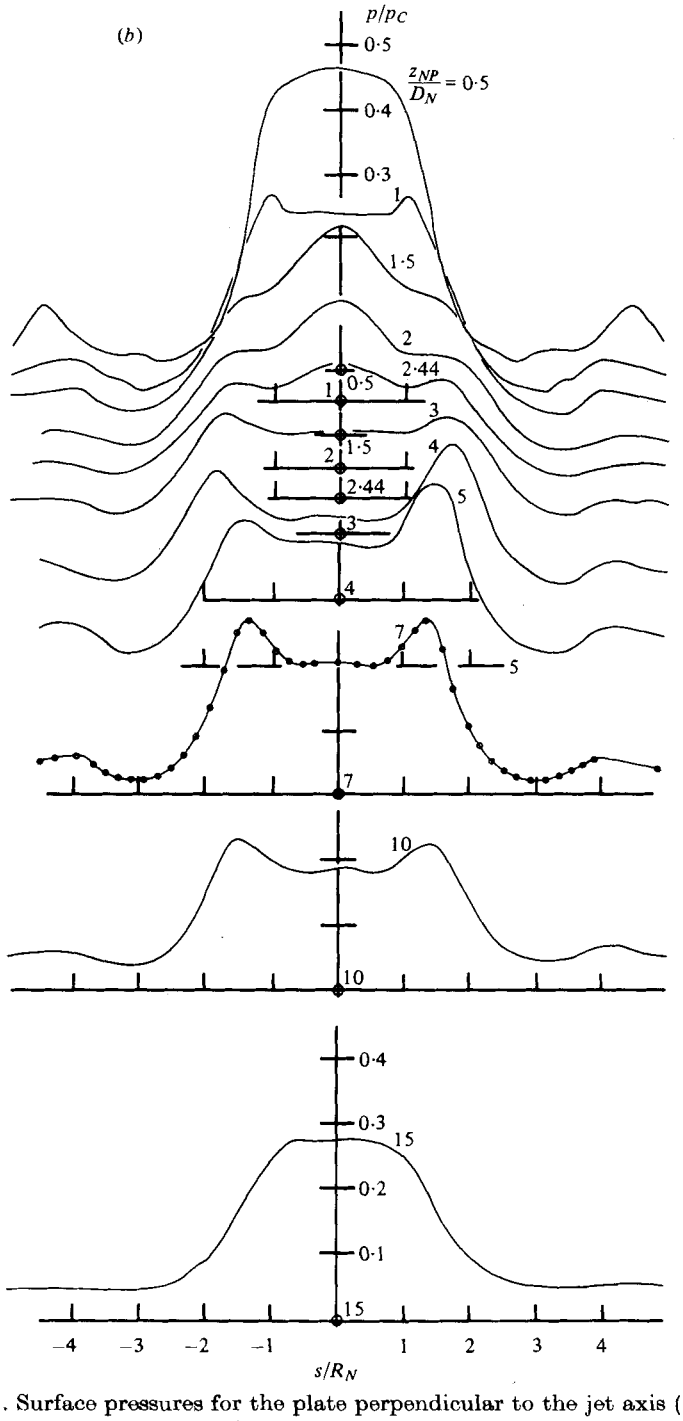

FIGURE 3. Surface pressures for the plate perpendicular to the jet axis ($\theta = 90°$). (*a*) $PR = 1·2$, (*b*) $PR = 2$.

jet edge by the plate and the upper shear layer of the wall jet (Carling & Hunt 1974). The shadowgraph of this flow (figure 4*a*) shows a plate shock which is convex upwards, again like the behaviour in a uniform jet.

Increasing z_{NP} to 1 diameter produces striking changes in both the pressures and the shock shapes. The level of pressure has fallen owing to the increased jet Mach number but the distribution in the shock layer region has altered also; the maximum pressure now occurs on a ring at a radius of $1{\cdot}2R_N$ inside of which the pressure is almost constant. This is a case where a stagnation bubble exists in the shock layer with attachment on the high pressure line. Kalghatgi & Hunt (1976) have shown that such bubbles are caused by a shock wave in the free jet which interacts with the plate shock, producing a curtain of air of high total pressure. It is this curtain that causes separation of the plate boundary layer. At $z_{NP} = D_N$, it is the nozzle shock (see § 3) which is responsible for the bubble. There is no bubble at the smaller plate separation of $z_{NP} = 0{\cdot}5D_N$ because, in this position, the nozzle shock intersects the plate shock too far from the axis for the curtain to influence the plate boundary layer. It is tempting to interpret the dome-shaped shock wave of figure 4(*b*) as being due to the presence of the bubble. This may be the case. However, the shadowgraphs for inclined plates (see § 7) contain domed shocks under conditions where the plate pressures show that the bubble has dispersed. Analternative explanation for the dome is that the shock is convex upwards in the central region, where the jet velocity varies only slowly and becomes flat in the outer region, where the expansion fan on the nozzle lip causes increasing Mach numbers and flows angle in the jet. A similar domed shock can be seen in figure 4 of the paper by Gummer & Hunt (1974) in a case where there is no bubble.

Further increase of z_{NP} moves the plate shock into a region where the nozzle shock crosses the axis of the free jet and the bubble disappears, to be replaced by a slight central hump in the pressure distribution; this is produced by the higher total pressure of the innermost flow which has passed through the reflected nozzle shock. Also visible in these pressure distributions is a growing ring of high pressure at a diameter of $1{\cdot}35D_N$ in the lower pressure ratio jet ($PR = 1{\cdot}2$) and $1{\cdot}6D_N$ in the other jet. This pressure rise is induced by the shear layer which originates at the intersection of the plate shock with the jet shock. As z_{NP} increases, the effect becomes greater because the intersection point moves inward and the strength of the jet shock rises. Eventually, the pressure rise becomes great enough to separate the plate boundary layer and cause the formation of another bubble. Figure 3 shows that this has occurred by $z_{NP} = 2{\cdot}44D_N$ in the $PR = 1{\cdot}2$ jet and by $z_{NP} = 3D_N$ in the $PR = 2$ jet. The later promotion of the bubble at the higher pressure ratio is due to the greater diameter of the jet shock which reduces the influence of the shear layer at a given plate location. Through this range of plate locations, the inner shock in the $PR = 1{\cdot}2$ jet remains almost flat while that in the $PR = 2$ jet is concave upwards. This concavity is generally found to occur when the shock lies in the expansion from the nozzle lip.

At larger values of z_{NP}, the plate lies in the second shock cell and, eventually, a plate shock forms below the Mach disk (see figure 4*c*). A bubble still exists in most of the flows, induced either by the jet shock in the cell or by the slip surface from the Mach disk. The flow fields become increasingly influenced by the mixing of the jet as z_{NP} increases until at $z_{NP} = 15$ diameters, the pressure distribution takes on a form characteristic of a subsonic jet.

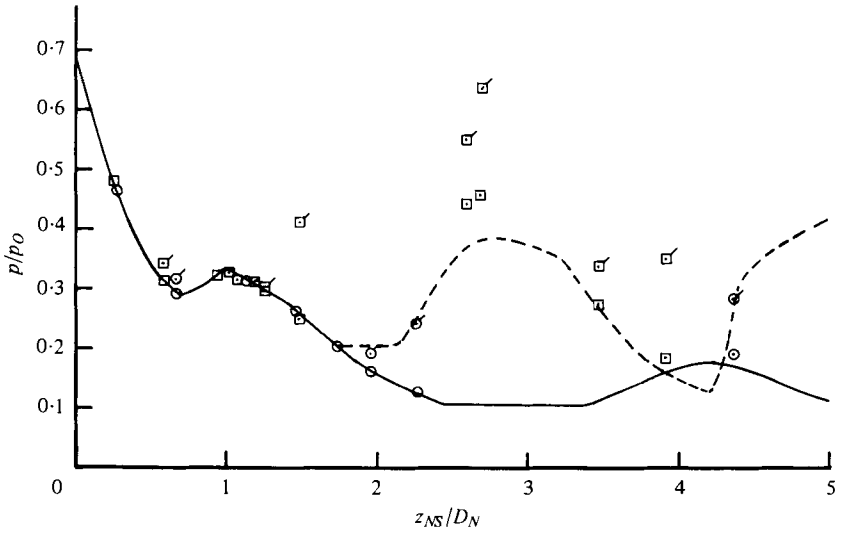

FIGURE 5. Central and maximum surface pressures for a perpendicular plate plotted against plate shock location and compared with free-jet pitot pressures. – – –, pitot pressure, $PR = 1{\cdot}2$; ——, pitot pressure, $PR = 2$; ⊡, central surface pressure, $PR = 1{\cdot}2$; ⊡, maximum surface pressure, $PR = 1{\cdot}2$; ⊙, central surface pressure, $PR = 2$; ⊙, maximum surface pressure, $PR = 2$.

A case worthy of further comment is that of the low pressure-ratio jet with $z_{NP} = 3$. It can be seen that the pressure levels are unusually high. The shadowgraph of this case (not presented) shows it to be in the second shock cell, with a plate shock just beginning to form downstream of the Mach disk, which is quite narrow in this jet. The high pressure levels are due to the mixing of the jet flow near the axis with the high total pressure air outside it, coupled with the plate shock being too weak to create significant shock losses. There is no corresponding case for the $PR = 2$ jet since the Mach disk is much larger and mixing is less effective.

6.2. *Correlations of some features*

Maximum pressures. In the case of a regular flow with no bubble and no mixing on the centre-line, the central pressure will be the free-jet pitot pressure corresponding to the location on the jet axis of the plate shock. This quantity has therefore been compared to the central and to the maximum plate pressures in figure 5. The figure shows the measured centre-line pitot pressures, replotted from figure 1. Also shown are the plate central and maximum pressures, plotted against the central location of the plate shock wave, z_{NS}. It can be seen that, within the first shock cell, the central plate and pitot pressures agree very well, even where there is a stagnation bubble present. At larger plate spacings, the agreement is also good except in the case of the lower pressure ratio jet for $z_{NP} = 3D_N$, where the measured plate pressure is substantially higher than the pitot pressure. This must be due to enhanced mixing in the region downstream of the plate shock. The maximum plate pressures can be much larger than the free jet pitot values, showing that the reattachment streamlines have mixed significantly with the higher total pressure outer flow.

Occurrence of stagnation bubbles. Kalghatgi & Hunt (1976), in their study of shock layer stagnation bubbles, proposed a parameter, D, whose value is an indication of whether or not a stagnation bubble will occur. According to Kalghatgi & Hunt, the

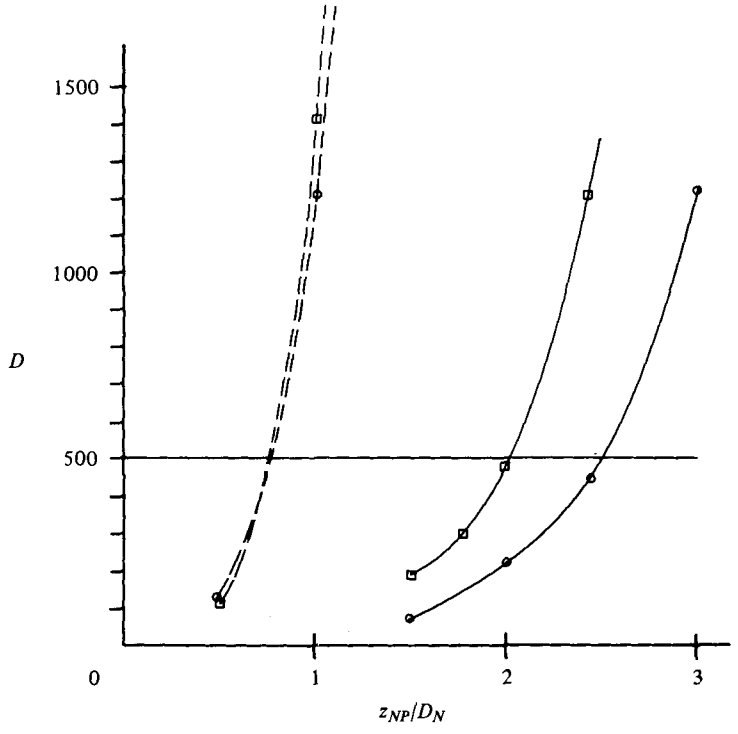

FIGURE 6. Variation of parameter D within the first shock cell. ⊡, $PR = 1{\cdot}2$; ⊙, $PR = 2$; ——, jet shock intersection; – – –, nozzle shock intersection.

mechanism of bubble formation involves the separation of the plate boundary layer by the pressure rise imposed by a shear layer, this being generated at the intersection of the plate shock with a weak shock in the free jet (see § 6.1). Their parameter D attempts to construct the ratio of the imposed pressure rise to that required to cause separation: D should therefore have a critical value above which a bubble occurs and below which regular flows occur. Kalghatgi & Hunt calculated the values of D for some 25 cases (mostly involving very weak jet shock waves) and found the critical value of D to be about 360. The variation of D was from 0 to 22800.

The evaluation of the quantity D requires that the strength and location of the intersecting shock should be known, this effectively limits the application to the first shock cell. Values of the parameter D have been calculated at points along the nozzle shock and along the jet shock using data from the Lockheed plume program (see § 3) and shock heights measured from the shadowgraphs. Figure 6 presents these values. The best choice of the critical value of D for the present series of tests is 500. This choice correctly predicts the nature of the flow in every case and suggests that the case $z_{NP} = 2D_N$ in the $PR = 1{\cdot}2$ jet (for which $D = 477$) should be regular but close to the formation of a bubble: the high outer peaks in the pressure distribution to be found in figure 3 confirm that this is correct. A value of 500 is clearly not in agreement with the value 360 found by Kalghatgi & Hunt. However, an examination of Kalghatgi & Hunt's cases shows that their results do not seriously conflict with a critical value of 500: the lowest value of D for which they report a bubble is 377 but their next value is 909. Adoption of a critical value of 500 thus results in only one incorrect prediction

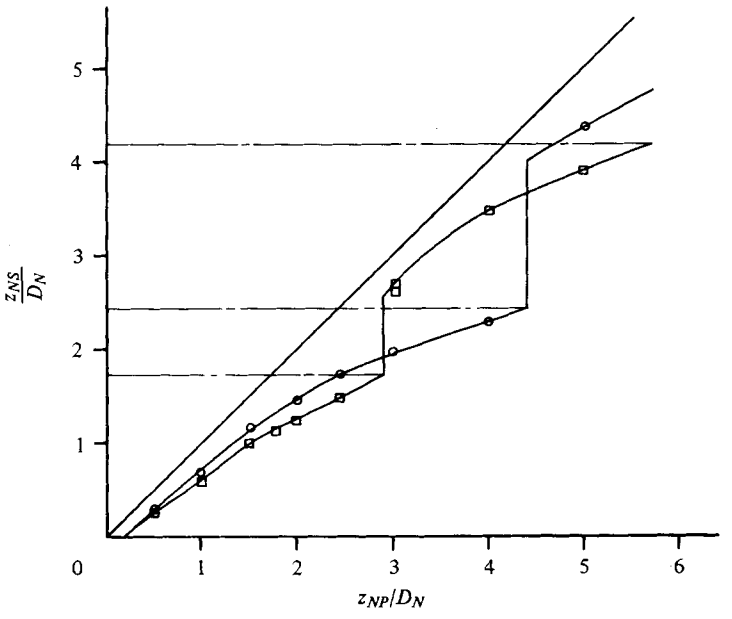

FIGURE 7. Variation of central plate shock location along the jet axis for a perpendicular plate. ⊡, $PR = 1{\cdot}2$; ⊙, $PR = 2$. – – –, Mach disk location.

out of the 35 cases examined by Kalghatgi & Hunt and in this work. This does not establish a universal critical value but nonetheless it is very satisfactory, particularly in view of the assumptions made in constructing the parameter D and the further assumptions which are often necessary to calculate it.

Plate shock location. The position, z_{NS}, along the jet axis of the centre point of the plate shock is shown in figure 7 where it is plotted against the plate location z_{NP}. The stand-off distance is then the vertical distance on the figure of the value of z_{NS} from the line of unit slope.

It can be seen that, as z_{NP} increases from $0{\cdot}5D_N$, the shock stand-off distance increases until the plate shock lies in the position of the first Mach disk. At this point, the flow between the Mach disk and the plate just achieves a sonic value. On further displacement of the plate, a region of supersonic flow appears and a new plate shock is generated at a finite distance from the plate but downstream of the Mach disk which remains in its free jet location. There is, therefore, a sudden increase in the plate shock location, z_{NS}. Subsequent passage of the plate through the second Mach disk position produces a similar behaviour.

Semiletenko & Uskov (1972) have offered a correlation of shock location within the first shock cell, based on the location of the Mach disk, z_{TM}, and using distances measured from the nozzle throat (for which the symbols z_{TM}, z_{TS} and z_{TP} are used) rather than from the exit plane. Their proposed curve is compared with the present data in figure 8. Also shown are three cases from Donaldson & Snedeker's (1971) work and three from Gummer & Hunt's (1974) work; these cases all used sonic orifices. It can be seen that the correlation is a useful one, although not within the scatter of the points shown in Semiletenko & Uskov's paper. The correlation can be improved somewhat if z_{TM} is replaced by that location of the plate in the second shock cell at

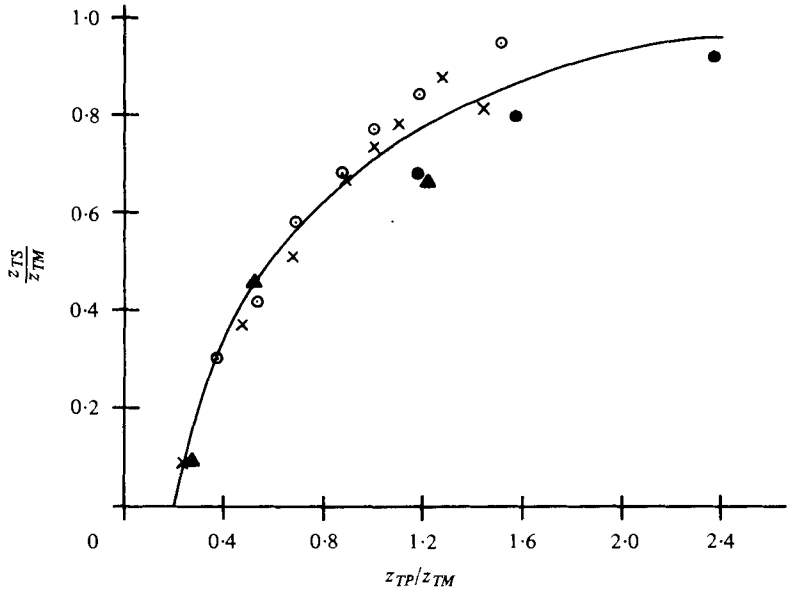

FIGURE 8. Variation of central shock location within the first shock cell for a perpendicular plate. ×, $PR = 1{\cdot}2$; ⊙, $PR = 2$; ●, Snedeker & Donaldson (1965); ▲, Gummer & Hunt (1971) sonic orifice; ——, correlation due to Semiletenko & Uskov (1972).

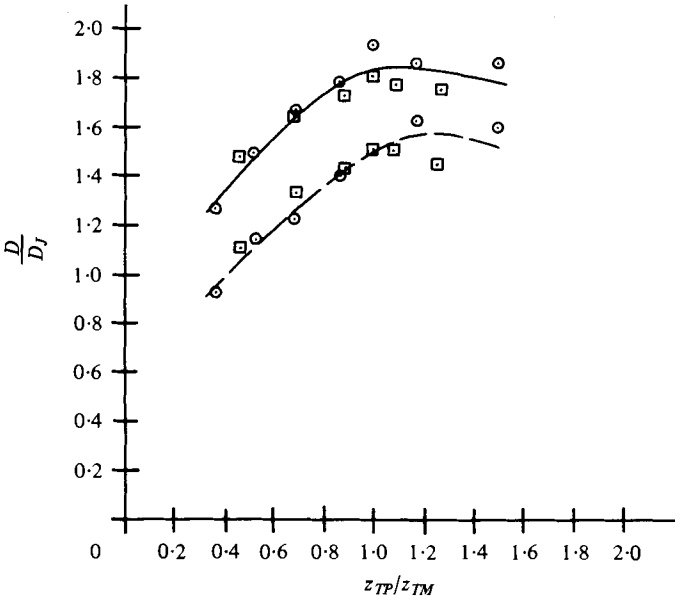

FIGURE 9. Variation of sonic point and atmospheric pressure location on a perpendicular plate. ⊡, $PR = 1{\cdot}2$; ⊙, $PR = 2$. ——, D_a; – – –, D_*.

which a new plate shock forms (Lamont & Hunt 1977). However, this quantity cannot be obtained directly from the free jet data and z_{TM} is preferred for convenience.

Diameter of impingement region. There are at least two useful ways to characterize the extent of the impingement region: by the diameter of the sonic point on the plate, D_*, and by the diameter at which the pressure first reaches the ambient value, D_a.

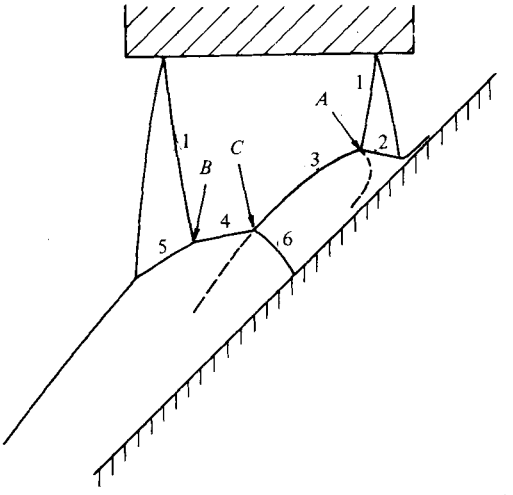

FIGURE 10. Shock nomenclature: A, upper triple point; B, lower triple point; C, intermediate triple point; 1, jet shock; 2, upper tail shock; 3, upper plate shock; 4, lower plate shock; 5, lower tail shock; 6, intermediate tail shock.

The sonic point is of particular significance to the structure of the flow, while the ambient point is of importance in considering the force on the plate.

If the diameter of the ambient point is plotted as a function of plate location, it is found that the diameter initially increases as z_{NP} increases, that it reaches a maximum somewhere in the first shock cell and then falls, to rise again in the second shock cell. The behaviour of the sonic diameter is very similar. It seemed possible that the behaviour of the ambient diameter might be related to the variation of the free-jet diameter, either at the plate location or the plate shock location. However, neither of these quantities is very successful in correlating the data. In view of the observation that the variation in D_a is related to the shock cell structure and since the distance z_{TM} had proved successful in collapsing the shock heights, it was decided to use this quantity to non-dimensionalize the plate location and to allow for the effect of underexpansion by means of the maximum diameter of the free jet, D_J. The results of this treatment are shown in figure 9 for both D_a and D_*. It can be seen that good correlation is achieved in the initial part of the shock cell but that it deteriorates somewhat thereafter.

7. The inclined plate

The pressure distributions and shadowgraph pictures obtained with a plate inclined to the jet axis in the angular range $30° \leqslant \theta \leqslant 90°$ are presented and discussed in this section. The locations of the more pronounced features of the pressure distributions are shown on the corresponding shadowgraphs to assist the discussion.

Many of the main features of the flows occur on the plane of symmetry and most of the discussion is concerned with this plane but some complete pressure footprints are presented and some three-dimensional effects are considered.

Subsection 7.1 is concerned with impingement in the first shock cell where analysis of the flows is possible, § 7.2 discusses a common feature of the near field shock structure in some detail and § 7.3 considers impingement at greater distances from the nozzle.

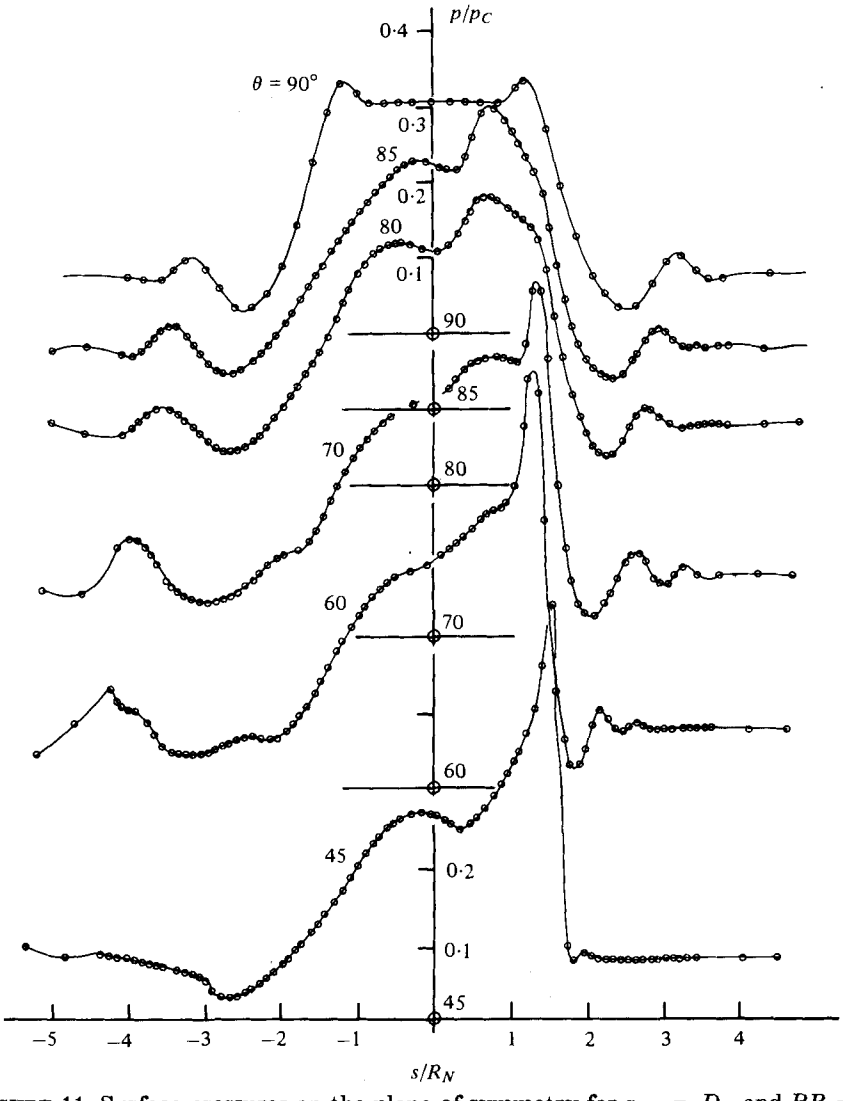

FIGURE 11. Surface pressures on the plane of symmetry for $z_{NP} = D_N$ and $PR = 1{\cdot}2$.

7.1. *Impingement in the first shock cell*

This section presents and discusses the results for cases where details of the free jet are available from the Lockheed plume program. These are $z_{NP} = D_N$ and $2D_N$ for $PR = 1{\cdot}2$ and 2 and $z_{NP} = 3D_N$ for $PR = 2$.

Wherever possible, analysis of the main features of the shock structure was carried out. Intersections were studied by the theories of shock confluence points due to Henderson (1966) and to Hunt & Lamont (1978). In these calculations, the local jet conditions and shock strengths were obtained from the Lockheed plume program; any other incident shock strengths were found by measuring shock angles on the shadowgraphs. Detailed results from these calculations will be referred to from time to time in the discussion but a general conclusion is that all the shock angles which

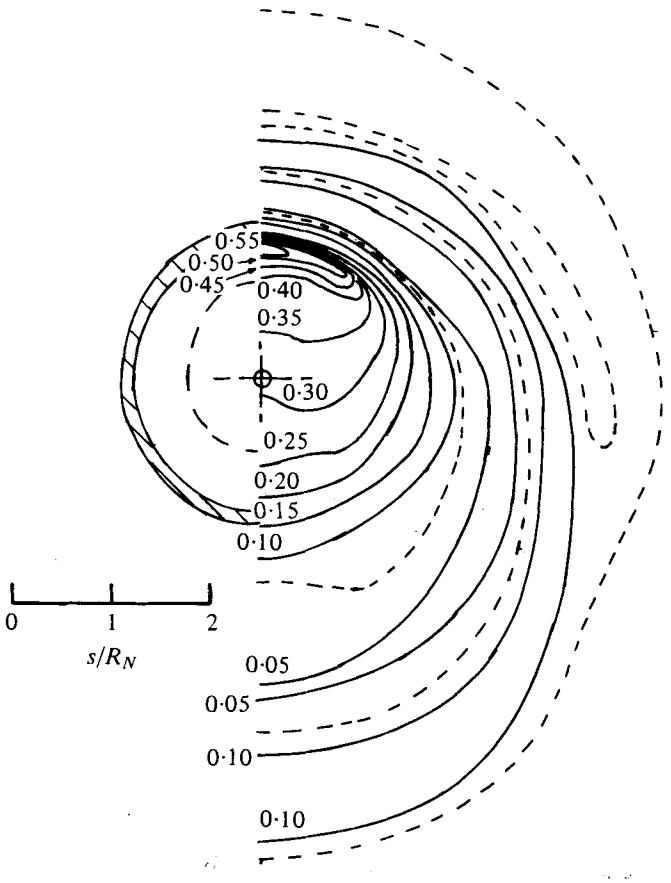

FIGURE 13. Surface pressure contours, p/p_C, for $z_{NP} = D_N$, $PR = 1{\cdot}2$ and $\theta = 60°$. — — —, $p_a/p_C = 0{\cdot}078$; ΣΣΣ, projection of free-jet edge; – – –, projection of free-jet shock.

were predicted agreed well with measurements from the shadowgraphs, except in one case in figure 25(*b*), which will be discussed later.

In the discussion of the flow fields which follows, frequent reference is made to the shock structure and it has been necessary to develop a terminology for the various shock components and their intersection points. Figure 10 shows a sketch explaining the nomenclature for three of the most common intersections. Further terminology will be developed as the flow patterns are encountered.

$z_{NP} = D_N$, $PR = 1{\cdot}2$: The pressure distributions in the plane of symmetry are shown for various values of θ in figure 11 and selected shadowgraph pictures in figure 12 (plates 3 and 4).

At $\theta = 90°$, a bubble exists due to the nozzle shocks but by $\theta = 80°$, the pressure distribution has changed considerably and it does not seem likely that a bubble is present, despite the domed shock shape of figure 12(*a*). The maximum pressure occurs much nearer to the jet axis than for $\theta = 90°$ and is slightly larger ($0{\cdot}39p_C$ compared to $0{\cdot}34p_C$). The location and magnitude are consistent with the stagnation streamline having passed through the flat region of the plate shock. There is a second pressure rise to a peak value of $0{\cdot}33p_C$ at $s = -0{\cdot}51R_N$ (where s is the distance from the jet axis measured up the plate). This is probably due to the high total pressure on the

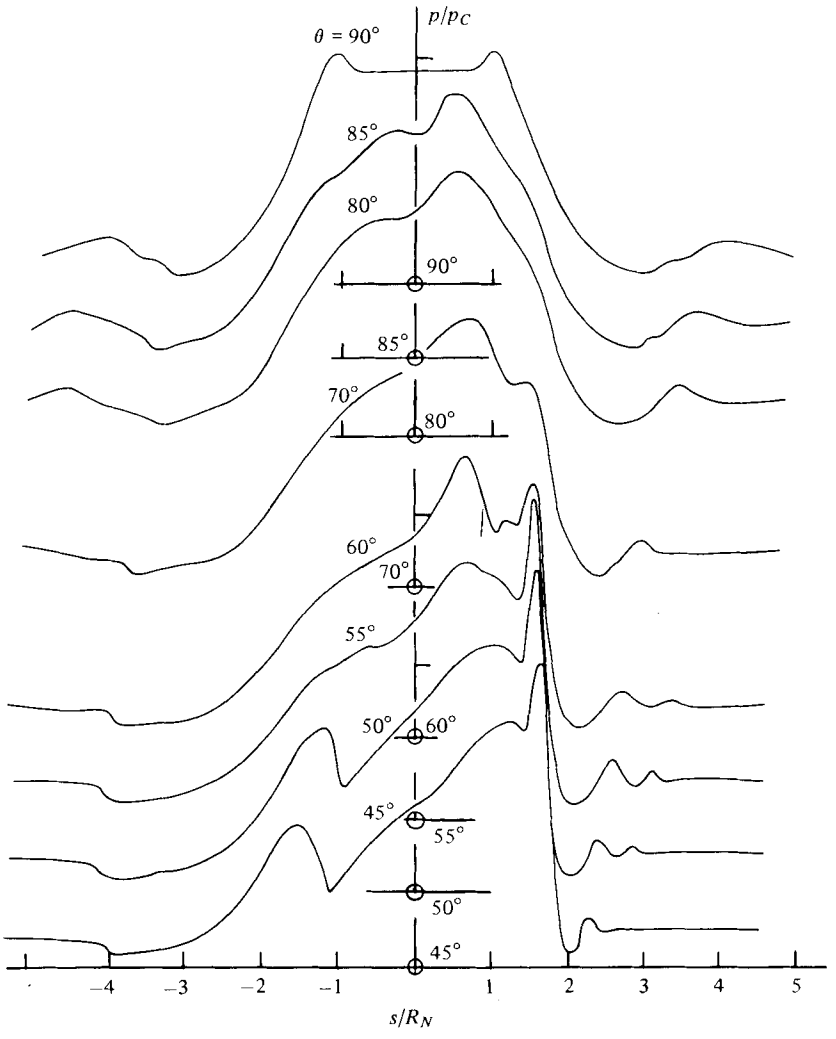

FIGURE 14. Surface pressures on the plane of symmetry for $z_{NP} = D_N$ and $PR = 2$.

slip line from the intersection of the nozzle shock with the plate shock. The slight inflexion in the upward flowing region is due to the slip line from the upper triple point. At $\theta = 70°$, the main pressure peak has increased in value to $0{\cdot}48p_C$ and moved out to $s = 1{\cdot}38R_N$. It is a development of the inflexion point which occurs for $\theta = 80°$ and is due to the movement of the stagnation streamline outside of the upper triple point (see figure 12*b*). Analysis of the conditions at the upper triple point gives a value of stagnation pressure of $0{\cdot}44p_C$ on the upper tail slip line. This flow is subsonic but the tail shock must subsequently weaken and become at least sonic at the jet edge (see Gummer & Hunt 1971). A consequence is that the total pressure rises as one crosses the upper tail flow towards the jet edge where the lowest possible value for inviscid flow is $0{\cdot}69p_C$. This is clearly much larger than the recorded peak and suggests that the stagnation streamline originates quite close to the upper triple point. The flow from the region of the plate shock which gave the stagnation point at higher values of θ now produces a slight hump in the pressure distribution with a maximum

value of $0{\cdot}37p_C$ at $s = 0{\cdot}70R_N$. When θ is reduced to 60°, the peak pressure rises to $0{\cdot}56p_C$ as the stagnation streamline moves outward but otherwise the pressure distribution and shadowgraph (not presented) are similar to those at $\theta = 70°$. At $\theta = 45°$, the peak pressure is slightly lower at $0{\cdot}54p_C$. It can be seen that a small new pressure hump occurs in the vicinity of the axis. The commencement of this hump agrees well with the location of a weak wave to be seen in figure 12(*c*). The wave is the weak tail shock of an intermediate triple shock intersection (see figure 10), which occurs part way along the plate shock, near the jet axis. Much more well-developed examples of the same shock structure can be seen in other figures (for example plate 25(*b*)) which will be discussed later.

An example of a pressure footprint in the form of a contour plot, is shown in figure 13, which applies to the case of $\theta = 60°$. The magnitude of s is shown as a scale. It can be seen that the high pressures associated with stagnation form a crescent-shaped ridge on the upper part of the plate. The lowest contours are somewhat elongated but those with intermediate values are almost circular, suggesting that there is significant lateral flow.

It was not possible to test lower plate angles than 45° at this value of z_{NP} because the plate then fouls the nozzle.

A general point of some importance which arises from these results is that the maximum pressure on an inclined plate can be considerably higher than that on a perpendicular plate: in the cases just considered, the largest pressure was 65 % above the perpendicular plate value and in other cases an increase as high as a factor of 3 was found. This is in contrast to the findings of Donaldson & Snedeker (1971) who found only the barest increase, even in the first shock cell. The reason for this discrepancy is that Donaldson & Snedeker's pressure distributions did not extend into the high pressure upper tail flow region, as may be seen from figure 2, and hence they failed to obtain the true peak values. For the same reason, their values of stagnation point displacement are also incorrect in the near jet. Note, however, that many of their results apply to regions where the jet is subsonic and are then valid. Among the complete set of results presented by Snedeker & Donaldson (1965), there are three cases of large pressure peaks on inclined plates. These were not of primary interest to their study and were not investigated further at that time.

$z_{NP} = D_N$, $PR = 2$: The pressure distributions from the plane of symmetry are presented in figure 14, experimental points on this and subsequent similar figures have been omitted for clarity: the resolution and scatter are similar to those on figure 11. Shadowgraph pictures for these flows may be found in figure 15 (plates 5 and 6).

As θ is reduced from 90°, the flow patterns initially follow the same sequence as for $PR = 1{\cdot}2$. A bubble exists at $\theta = 90°$ but has disappeared by $\theta = 85°$ when the stagnation streamline passes through the flat part of the plate shock, see figure 15(*a*). The influence of the upper tail region can be seen to grow as θ is reduced below 80°. Checking the plate pressures produced by the upper tail flow against the total pressure levels which are calculated to be present shows that the stagnation streamline first moves into the upper tail flow at $\theta = 55°$. It can be seen from the shadowgraph, figure 15(*b*), that an intermediate triple point (see figure 10 for the terminology) is formed at this angle; there is no intermediate triple point at $\theta = 60°$. In the case of figure 15(*b*) the intermediate tail shock does not penetrate as far as the plate because the flow immediately above the plate is subsonic. It does, however, give rise to the

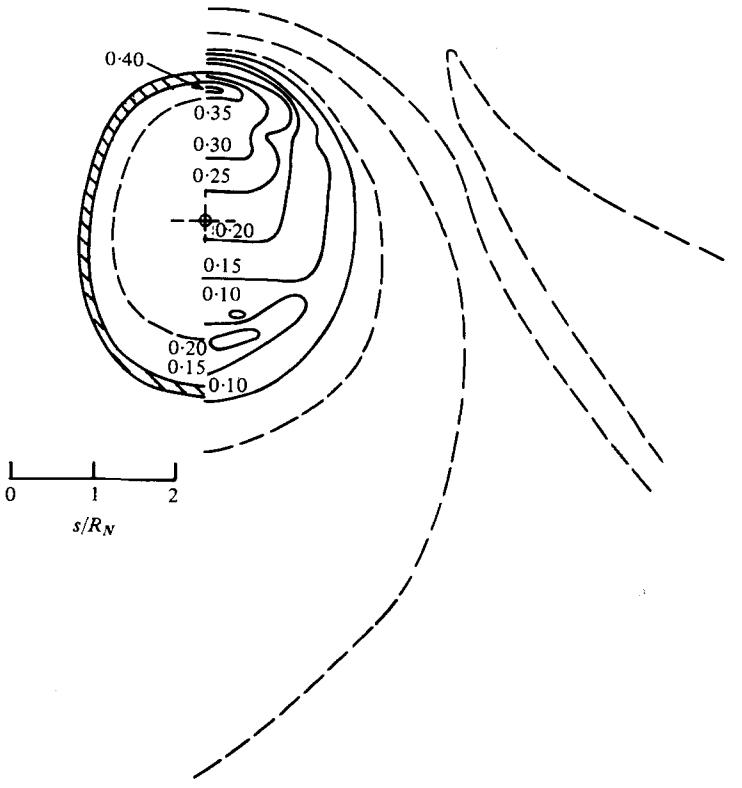

FIGURE 16. Surface pressure contours, p/p_C, for $z_{NP} = D_N$, $PR = 2$ and $\theta = 45°$. — — —, $p_a/p_C = 0{\cdot}046$; ⩩, projection of free-jet edge; – – –, projection of free-jet shock.

slight inflexion in the pressure distribution which can be seen in figure 14. At $\theta = 50°$, the only change is that the intermediate tail shock now reaches the plate, as seen in figure 15(*c*), and produces a sharp pressure rise. The situation at $\theta = 45°$ is similar. The complete footprint for this case is presented in figure 16 where it can be seen that the stagnation ridge is very limited in extent but the shock induced pressure rise extends laterally to approximately the maximum width that the jet shock has at this location.

Comparing the results for the two pressure ratios one finds the same sequence of flow patterns as θ is reduced, but with two noticeable differences. Firstly, the value of θ at which the stagnation streamline moves into the upper tail flow is much smaller in the high pressure ratio jet (about 57° compared to about 77°). This is most likely due to the higher flow angles in the free jet and to the greater diameter of the jet shock. The second difference is that the intermediate triple point first occurs at a higher value of θ and becomes more well developed when a pressure ratio of 2 is used. The reason for this is that an intermediate triple point requires the plate shock to be weak over its lower section and this is more readily achieved at the higher pressure ratio since then the flow in the lower part of the free jet is inclined further outwards and therefore makes a smaller angle with the plate.

$z_{NP} = 2D_N$, $PR = 1{\cdot}2$: The pressure distributions in the plane of symmetry are presented in figure 17 and selected shadowgraphs in figure 18 (plates 7 and 8). The

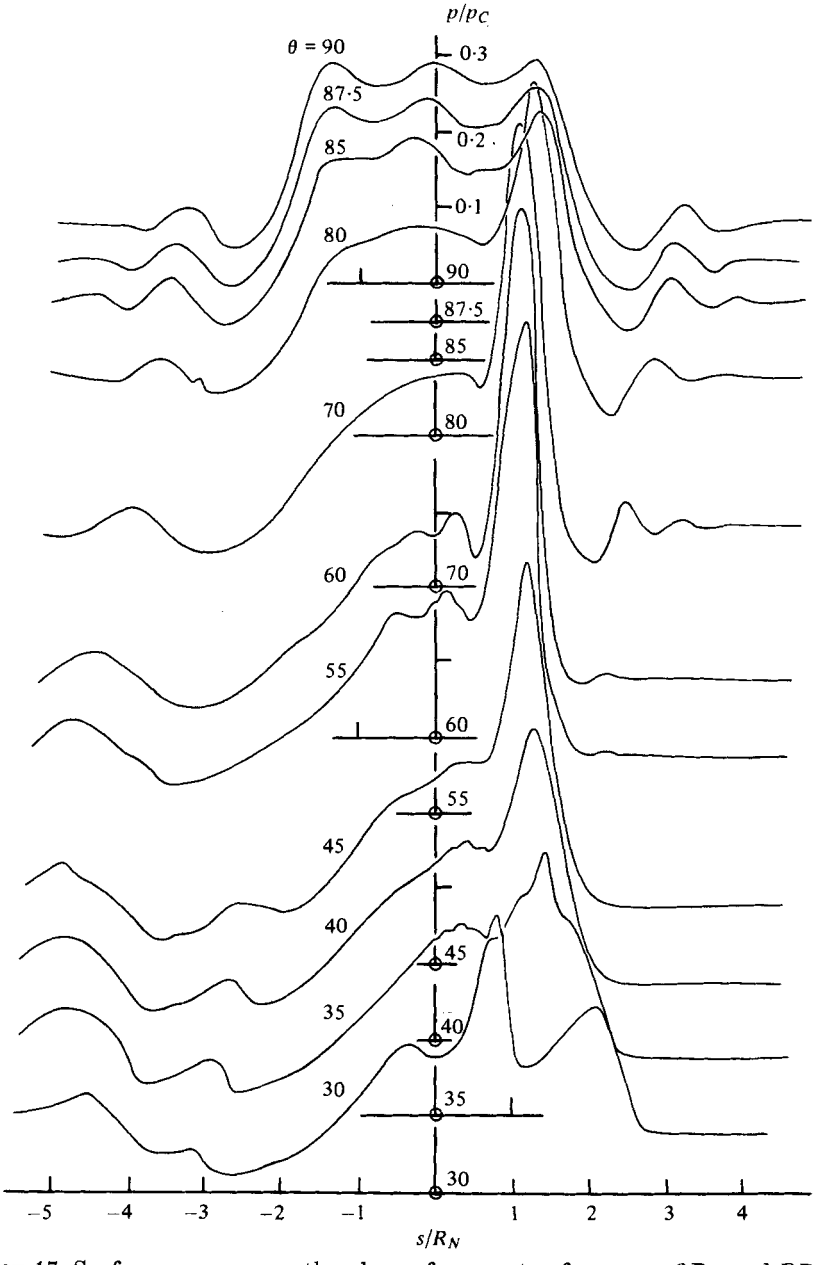

FIGURE 17. Surface pressures on the plane of symmetry for $z_{NP} = 2D_N$ and $PR = 1{\cdot}2$.

influence of the triple points caused by the jet shock is evident even at 90° but it appears that θ must be reduced to 70° before the stagnation streamline moves into the upper tail flow. This can be seen when the stagnation pressures in the tail region are calculated: the upper tail slip line is supersonic with a stagnation pressure of $0{\cdot}56p_C$. Assuming this flow passes through a normal shock before reaching the plate only reduces the pressure to $0{\cdot}55p_C$ compared to measured peaks of $0{\cdot}33p_C$ at 85° and $0{\cdot}48p_C$ at 80°. Moving outwards, the stagnation pressure just downstream of the tail shock rises but near the jet edge a new effect starts to operate. This is the expansion

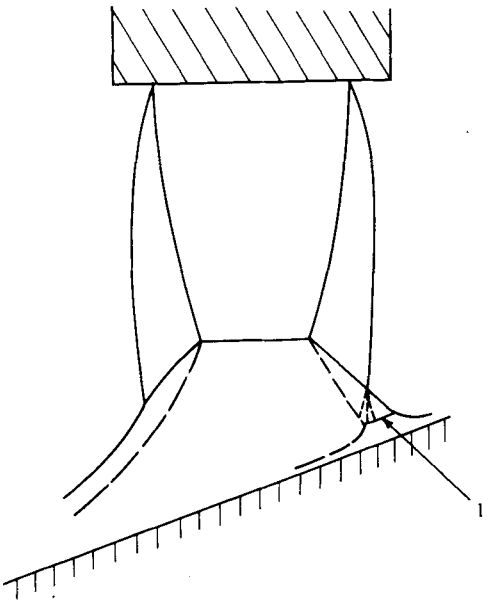

FIGURE 19. Sketch based on figure 18(*a*). 1, sub-tail plate shock.

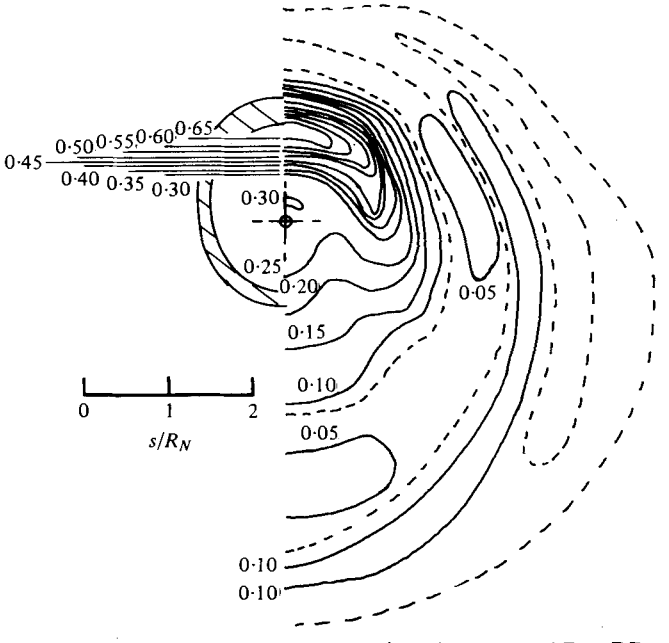

FIGURE 20. Surface pressure contours, p/p_C, for $z_{NP} = 2D_N$, $PR = 1{\cdot}2$ and $\theta = 60°$, legend as figure 13.

fan which is generated by the intersection of the tail shock with the jet edge. The effect of the expansion is to increase the Mach number of the flow and hence to increase the loss of total pressure through any terminal shock. However, the magnitude of this effect at the jet edge can be calculated and gives a total pressure of $0{\cdot}56p_C$, again much larger than the measured peak, even at $\theta = 80°$. At $\theta = 70°$, the upper peak

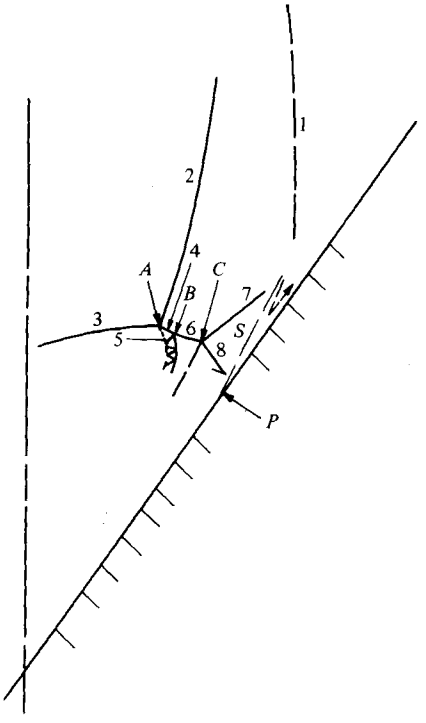

FIGURE 21. Reconstruction of upper tail flow at figure 18(*c*). *A*, upper triple point; *B*, inner secondary triple point; *C*, outer secondary triple point; 1, jet edge; 2, jet shock; 3, upper plate shock; 4, upper tail inner shock; 5, inner secondary tail shock; 6, upper tail mid shock; 7, leading plate shock; 8, outer secondary tail shock. *P*, location of peak pressure. *S*, stagnation streamline.

pressure has risen to $0{\cdot}63p_C$ and this must be the stagnation point, the stagnation streamline having originated some little way outside of the upper triple point and been brought to a subsonic value by a strong sub-tail plate shock. A sketch showing this shock wave can be seen in figure 19. The sketch is based on the shadowgraph, figure 18(*a*). However, it can be seen that there is no conclusive evidence in the shadowgraph for the existence of the sub-tail plate shock: the figure only contains a dark and rather blurred region where the shock might be expected to lie. Indeed, it has generally turned out to be difficult to obtain detail of the upper tail flow region. At least in part this is due to the jet edge and upper triple point shear layers which create turbulence and diffuse the wave systems.

Reducing the plate angle to 60° produces a rise in the peak pressure to $0{\cdot}69p_C$ but otherwise little change. A contour plot of the footprint is presented in figure 20. The very high, crescent-shaped stagnation ridge can be clearly seen. Note that it extends down the plate for a distance of about one jet radius, consistent with the extent of the dark, blurred regions seen on the shadowgraphs (see figure 18*a*).

There is little change by $\theta = 55°$ but at $\theta = 45°$, a new upper tail shock pattern appears and persists at $\theta = 40°$ and 35°, for which shadowgraphs are presented in figures 18(*b*, *c*) respectively. The form of the pressure distribution changes slowly as the peak pressure drops from $0{\cdot}66p_C$ at $\theta = 55°$ to $0{\cdot}35p_C$ at $\theta = 35°$, and a hump develops just above the axis. Figure 21 shows a reconstruction of the upper tail flow

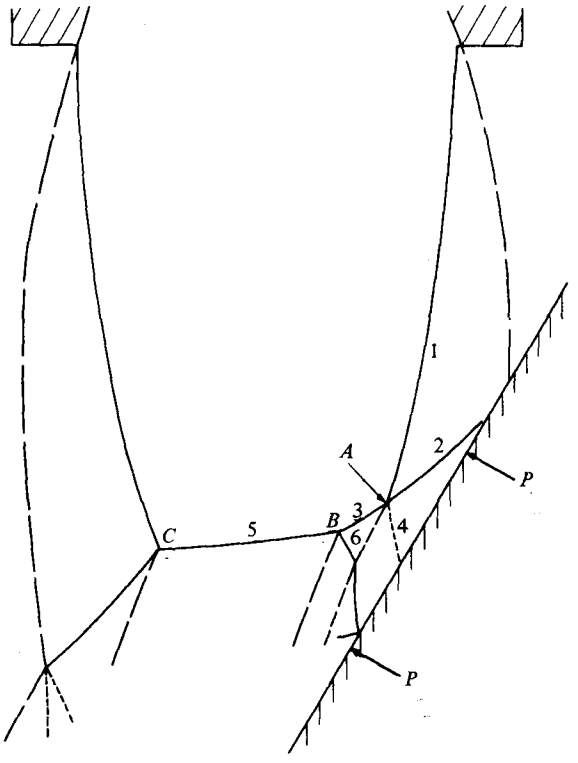

FIGURE 22. Reconstruction of figure 18(*d*). *A*, same-family confluence; *B*, intermediate triple point; *C*, lower triple point; 1, jet shock; 2, leading plate shock; 3, upper plate shock; 4, secondary expansion; 5, lower plate shock; 6, intermediate tail shock. *P*, maximum pressures.

at $\theta = 35°$ (see the shadowgraph of figure 18*c*) and sets out the terminology for this shock structure. The reconstruction was arrived at by means of triple point solutions at *A*, *B* and *C* using the Lockheed plume program for upstream flow conditions and the jet shock strength. The incident shock strength at *B* was taken to be equal to the predicted upper tail shock strength; the angle of the leading plate shock (which acts as the incident shock at *C*) was obtained by measurement from the shadowgraph. All other shock and slip line directions at the triple points of figure 21 were calculated. When comparing figure 21 with figure 18(*c*), note that the slip line from the outer secondary triple point is a little confusing since it appears black on the shadowgraph: the corresponding slip line on figure 18(*b*) is more easily identified.

The shock structure of figure 21 consists of a double triple point within the upper tail shock. It is created by the interaction of a weak leading plate shock and a weak tail shock propagating from the upper triple point. The inner secondary tail shock of figure 21 (numbered 5) is very short and propagates across the upper tail inner flow to the upper triple point slip line. The flow downstream of the upper plate shock is subsonic and the wave reflects. Thereafter it reflects repeatedly between the upper triple slip line and the inner secondary slip line, turning the flow towards the jet centre line on each occasion. The inner secondary tail flow is therefore a narrow supersonic jet embedded between two subsonic flows (compare the embedded jets identified by Edney (1968) in his superb study of shock impingement heating). The peak plate pressure for these cases presents a puzzle. At $\theta = 35°$, it has a value of

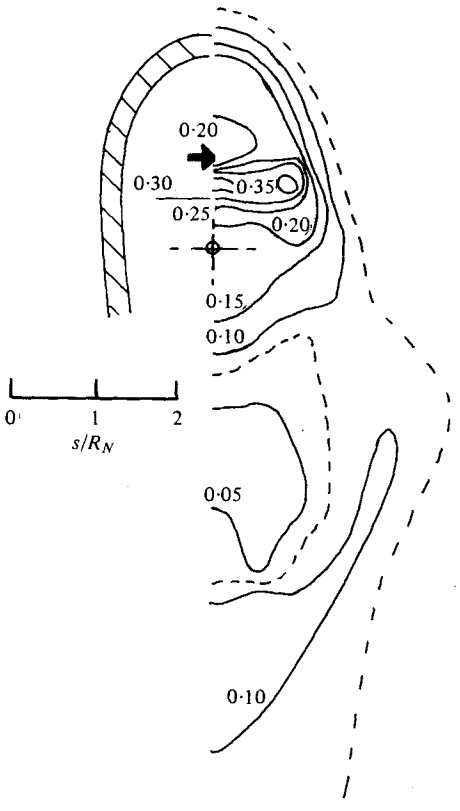

FIGURE 23. Surface pressure contours, p/p_C, for $z_{NP} = 2D_N$, $PR = 1{\cdot}2$ and $\theta = 60°$. →, location of impinging shock from shadowgraph; remaining legend as figure 13.

$0{\cdot}35p_C$ which is substantially below the lowest calculated stagnation pressure downstream of the upper tail shock system: this is $0{\cdot}44p_C$ and is in the upper tail mid flow. Furthermore, it is quite clear from figures 18(*b*, *c*) that the peak lies in the outer secondary tail flow, whose calculated stagnation pressure is about $0{\cdot}69p_C$. Now, the plate angle is greater than the shock detachment angle for the outer flow so that the low value of peak pressure cannot be due to the leading plate shock being attached. A possible explanation for this curious behaviour is that the peak plate pressure is produced by a stagnation point formed from the flow in the *edge shear layer*, where the total pressure has been reduced by mixing. The measured peak value ($0{\cdot}35p_C$) is remarkably close to the calculated *static* pressure ($0{\cdot}36p_C$) at the outer secondary triple point; thus it may be the level of the static pressure in the flow above the plate that determines which part of the shear layer supplies the stagnation streamline. In general, it has been found at low plate angles that the edge shear layer has a considerable influence on the upper tail flow by allowing a weak leading plate shock to exist where it could not occur in an inviscid flow. In such a case there will naturally be very little fluid flowing up the plate. The small pressure hump just above the axis when $\theta = 40°$ and 35° can be seen from the shadowgraphs in figures 18(*b*, *c*) to be due to the high total pressure of the embedded supersonic jet.

When the plate angle is reduced further to 30°, yet another type of shock pattern

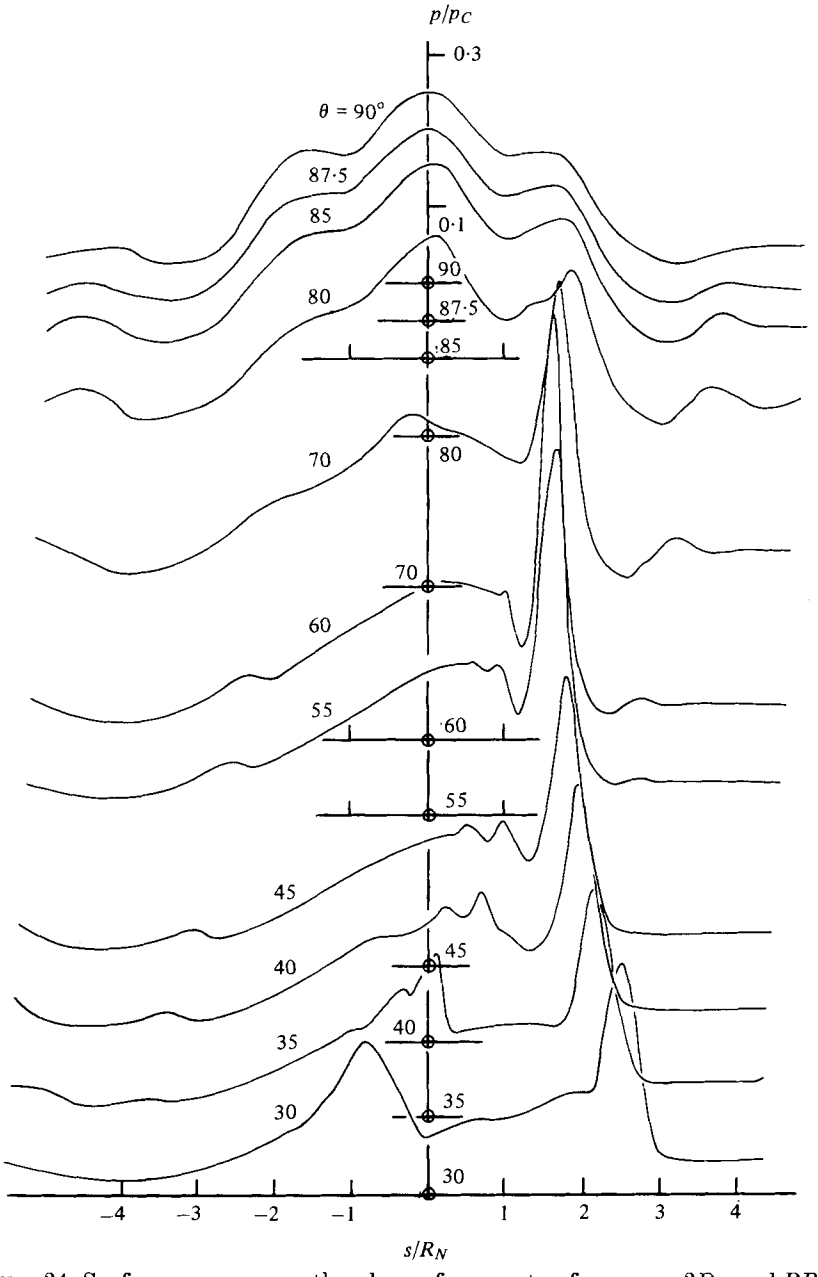

FIGURE 24. Surface pressures on the plane of symmetry for $z_{NP} = 2D_N$ and $PR = 2$.

occurs, as shown by figure 18(*d*). Figure 22 is a reconstruction of this flow using calculated conditions from shock intersection theory wherever possible. The upper triple point has disappeared and has been replaced by a same-family confluence between the jet shock and the leading plate shock, these two combining into a weak upper plate shock. This shock then forms an intermediate triple point where a strong lower plate shock is produced which curves slightly and spans the gap to the lower triple point. The intermediate tail shock is propagated to the plate, crossing a slip

line from the same family confluence en route. Reflexions of this wave between the plate and the slip line can be seen. The central plane pressure distribution for this case can be seen in figure 17. It has two notable features. The first is the low value of the upper pressure peak ($0{\cdot}25p_C$). The second is the sharp pressure rise at $s = 0{\cdot}8R_N$. This second feature is due to the intermediate tail shock: figure 18(*d*) shows the good correlation of the location of the pressure rise with the shock impingement position. The subsequent rapid fall in pressure is due to the reflected wave which is an expansion. Turning now to the upper peak, the maximum value is much less than the calculated stagnation pressures produced by the leading plate shock. An attached leading plate shock at the conditions of the inviscid jet edge is not possible but further inboard the Mach number is higher, the flow is directed slightly inward and it becomes possible to have a weak leading plate shock which deflects the flow parallel to the plate. Taking a point which is situated on the perpendicular from the upper plate pressure peak, it is found that such a shock is possible and that the required shock angle is consistent with the shadowgraph. Further, the static pressure produced by the shock is $0{\cdot}25p_C$, identical with the measured peak. The upper peak therefore again seems to be a stagnation region involving the edge shear layer, the pressure magnitude being determined by the static pressure at the shock above the plate. The contour plot of this case is presented in figure 23. The footprint can be seen to be highly elongated. The main pressure ridge, which is due to the intermediate tail shock is remarkably straight.

A comparison of the above results with those at $z_{NP} = D_N$ and $PR = 1{\cdot}2$ shows a number of new flow patterns, due in part to the smaller plate angles which can be achieved at $z_{NP} = 2D_N$. The other main cause of difference is the increased strength of the jet shock: this in turn gives rise to a weak upper tail shock from which two consequences arise. Firstly the stagnation pressure in the upper tail flow is greater and a maximum pressure of $0{\cdot}71p_C$ is reached (at $\theta = 60°$) compared to a maximum of $0{\cdot}56p_C$ when $z_{NP} = D_N$, which also occurs at 60°. The other result of having a weak tail shock is that it adjusts less readily to the changing location of the upper part of the plate and new interactions involving a leading plate shock are produced. A final point of difference is that the edge shear layer is thicker and starts to exert an influence.

$z_{NP} = 2D_N$, $PR = 2$: The pressure distributions are presented in figure 24 and the shadowgraphs in figure 25 (plate 9).

It can be seen that for a perpendicular plate, the flow is regular in the shock layer with some influence of the triple point showing in the pressure distribution. As the angle θ is decreased, the changes in flow pattern initially follow the same sequence as for the $PR = 1{\cdot}2$ jet: the stagnation streamline remains within the inner flow until $\theta = 70°$, when it moves to the upper tail flow. The maximum pressure, having risen dramatically at $\theta = 70°$, increases further at $\theta = 60°$ but then falls at $\theta = 55°$. This is accompanied by the occurrence of an inner secondary triple point which is just visible in figure 25(*a*) but it is not clear whether there is an outer secondary triple point, as in figure 21, or whether the bow shock simply forms a strong leading plate shock. At $\theta = 45°$, there is an indication on the shadowgraph (not presented) of an outer secondary triple point and the stagnation point either comes from the mid-tail shock or from the edge shear layer. At 40°, the inner plate shock weakens and forms an intermediate triple point similar to that seen in figure 15(*c*), the tail shock of which affects the subsonic flow over the plate sufficiently to produce the small humps seen on the pressure distribution. At $\theta = 35°$ and $\theta = 30°$, most of the flow over the plate

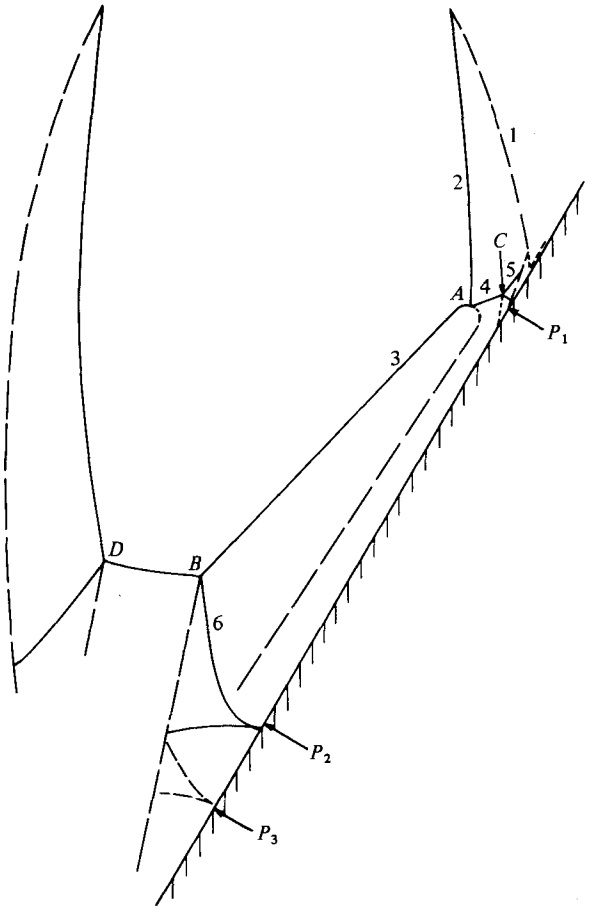

FIGURE 26. Reconstruction of figure 25(*b*). *A*, upper triple point; *B*, intermediate triple point, *C*, outer secondary triple point; *D*, lower triple point; 1, jet edge; 2, jet shock; 3, upper plate shock; 4, upper tail shock; 5, leading plate shock; 6, intermediate tail shock. P_1, stagnation point; P_2, pressure minimum; P_3, pressure maximum.

becomes supersonic and the intermediate tail shock reaches the plate, producing the sharp rises in pressure which can be seen in figure 24. At $\theta = 30°$, the striking shadowgraph of figure 25(*b*) is produced. The structure is in some respects similar to that of figure 22 but the intermediate triple point now occurs much lower down the plate. The fairly rapid drop in plate pressure which follows the shock-induced rise is due to the reflected expansion wave which can be clearly seen in figure 25(*b*). The details of the upper tail flow are not clear but they do seem to differ from those of figure 22. The jet shock is sufficiently weak that the upper tail flow is calculated to be just subsonic at the triple point. This means that an inner secondary triple point is not necessary and the inner part of the upper tail shock is strong. Now, this shock cannot bend and become weak in its outer section since this would require the upstream passage of information in the supersonic outer region. It seems more likely that an outer secondary triple point exists: one is just visible on an alternative shadowgraph and there is a faint but unmistakable tail shock for $PR = 1{\cdot}8$ at this plate angle. The inviscid flow is not capable of forming an attached leading plate shock and the

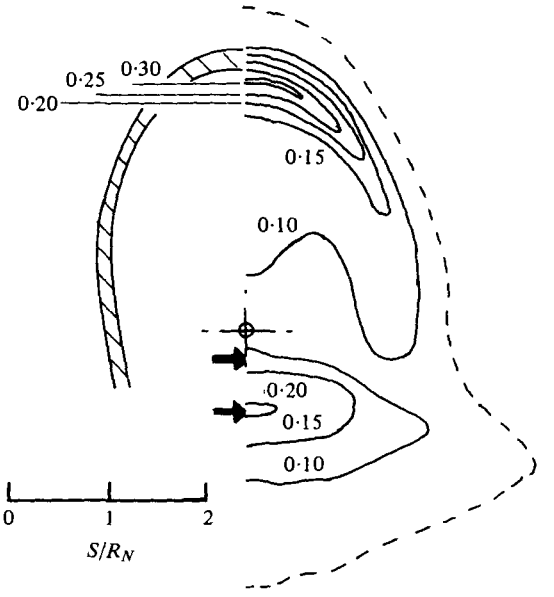

FIGURE 27. Surface pressure contours, p/p_C for $z_{NP} = 2D_N$, $PR = 2$, $\theta = 30°$. →, location of impinging shock from shadowgraph; remaining legend as figure 16.

structure in this vicinity is conjectured to be similar to that shown in figure 21 with the stagnation point being formed by a streamline which originates from within the edge shear flow. A three-shock confluence analysis for the postulated outer secondary triple point gives a value of static pressure just downstream of the triple point which equals $0{\cdot}30p_C$, equal to the measured peak: once again the choice of the shear layer streamline which forms the stagnation point seems to be governed by the static pressure above the plate. (Note, however, that this very close agreement with the triple point static pressure must be fortuitous since the angle of the leading plate shock cannot be measured with any accuracy.) A reconstruction of the flow pattern based on calculated intersection points is presented in figure 26. A point which is a little worrying is that the calculated shock angles at the upper triple point (A) are not in agreement with those seen on the shadowgraph. Since on all other occasions the triple point analysis has proved reliable, it is conjectured that it is also valid here but that the shock curvatures are large and the shock waves rapidly take up the inclinations seen on the photograph: this behaviour has been incorporated in figure 26. An associated rapid curvature of the slip line is also shown: a photograph taken for $PR = 1{\cdot}8$ shows this slip line more clearly. The suggested path of the slip line can be compared to that of the embedded supersonic jet which occurs in figure 21.

The pressure contours for $\theta = 30°$ are presented in figure 27. The lateral extent of the high pressure footprint can be seen to be confined to within a distance which is little more than the free jet width. It is also clear from the straightness of the contours near the plane of symmetry that the flow is indeed locally two-dimensional there so that three-dimensional effects cannot be the explanation of the behaviour in the upper tail flow. However, it will be argued in § 7.2 that three-dimensional effects are important to the shock structure further down the plate.

A comparison with the results for $PR = 1{\cdot}2$ shows that, as when $z_{NP} = D_N$, an

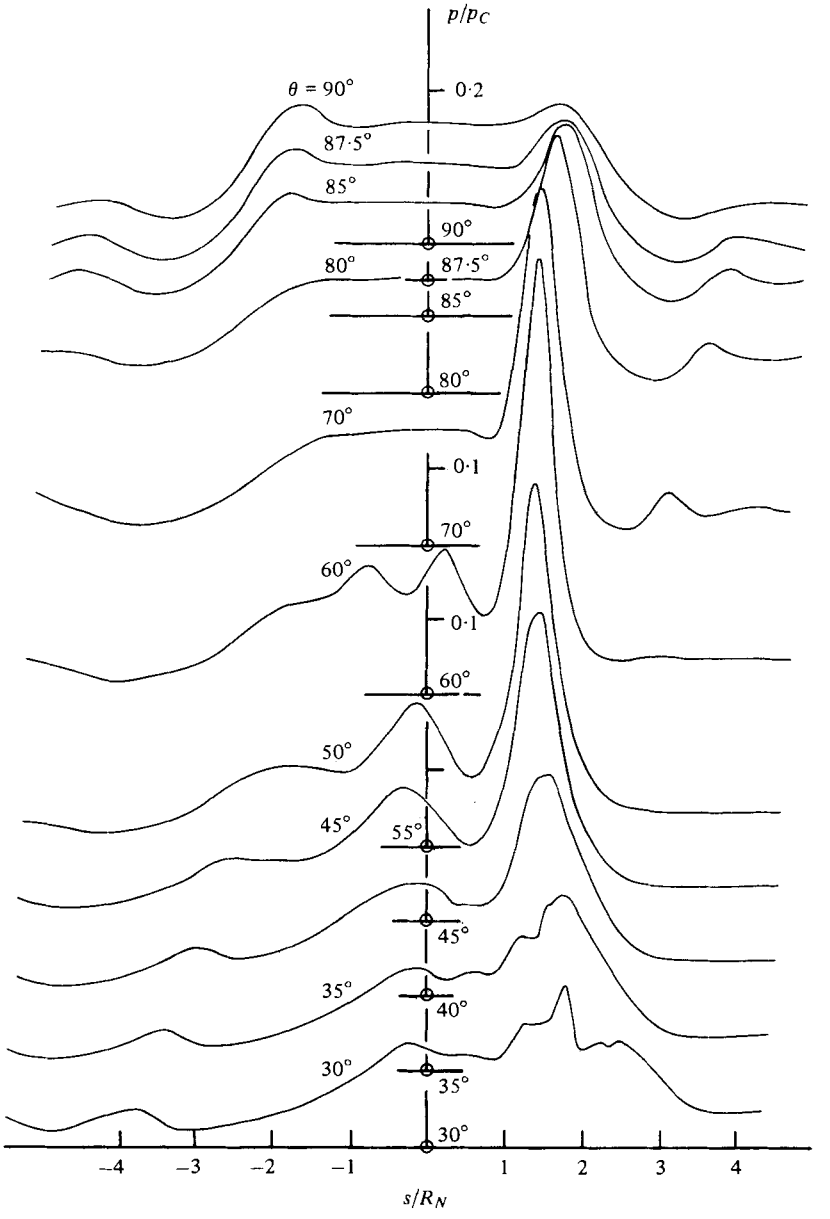

FIGURE 28. Surface pressures on the plane of symmetry for $z_{NP} = 3D_N$ and $PR = 2$.

intermediate triple point forms more readily due to the more favourable flow direction over the lower part of the shock system. In the upper tail flow, however, the larger flow angles inhibit the formation of a leading plate shock and the interactions are less complex although, again, the influence of the edge shear layer is important.

$z_{NP} = 3D_N, PR = 2$: At this pressure ratio, the first Mach disk occurs at $z_{NM} = 2{\cdot}44D_N$ but the downstream inner flow is still subsonic at $z_N = 3D_N$. Consequently, the Mach disk and its associated tail shocks are displaced upstream by the plate and become the plate shock system. The centre-plane surface pressures are presented in

figure 28. The shock structures are all of forms that have been encountered at lower values of z_{NP} and only one shadowgraph is presented; this is for the case $\theta = 30°$ and may be found in figure 29 (plate 10). In general, at this value of z_{NP}, the shear layers are thicker and their influence more pronounced.

For $\theta \geqslant 80°$, the flows are unsteady and the shadowgraphs indistinct. The pressure distributions show that a bubble exists at $\theta = 90°$ and persists until $\theta = 85°$. At $\theta = 80°$, the location of the stagnation point shows that the stagnation streamline comes from the upper tail flow but it must have been subjected to mixing because the peak pressure of $0{\cdot}35p_C$ is much less than the calculated values in the upper tail flow, the lowest of which is $0{\cdot}44p_C$. As θ falls, the upper half of the plate rises but the upper triple point remains almost stationary. A consequence of this is that the influence of mixing decreases and the peak pressure rises to a maximum of $0{\cdot}59p_C$ at $\theta = 60°$. In these flows, a sub-tail plate shock must exist (see figure 19). When θ is lowered further, the peak value starts to reduce due to a restructuring of the upper tail flow. The shadowgraphs are very indistinct in this region but the new shock structure probably takes the form of a leading plate shock and inner and outer secondary triple points (compare with figure 21). By $\theta = 30°$, this system has become established and may be seen in figure 29. An attached leading plate shock is possible on inviscid theory and the corresponding static pressure agrees well with the measured constant level seen in figure 28 just outboard of the main peak. However, it can be seen in figure 29 that the leading plate shock is not in fact attached to the plate, the explanation is that, again, the jet edge shear layer is responsible: it probably forms a stagnation point from a streamline whose total pressure equals the inviscid static pressure. The sharp pressure rise is clearly due to the outer secondary tail shock.

7.2. *The occurrence of intermediate triple points*

A detail which warrants discussion is the question why the interaction of a weak upper plate shock with the lower branch of the jet shock should always result in an intermediate triple point rather than in a simpler regular crossing of the plate and lower jet shocks: in addition to the cases presented here, the effect of further changes in pressure ratio and in plate angle was investigated; it was found that the intermediate triple point always appeared in preference to a regular crossing.

As a specific case, consider figure 25(*b*), the centre plane of which has been reconstructed in figure 26. An obvious explanation for the occurrence of the intermediate triple point is that a regular crossing of the shocks may be ruled out by shock confluence theory. This possibility was therefore investigated. In order to study the interaction of the plate shock with the lower branch of the jet shock, the plate shock must be extrapolated beyond the intermediate triple point. Two methods of extrapolation were used; namely a straight shock and a shock for which the deflected flow is parallel with the plate (both methods agree quite well with the form of the shock up to the intermediate triple point). In each case, the predicted plate shock strength is such that shock intersection theory allows a regular shock crossing to occur. Furthermore, the overlap of the shock polars is so large that it is most unlikely that the nature of the result is affected by the method of extrapolating the plate shock. An alternative explanation is therefore required.

The correct explanation is believed to lie in the three-dimensional part of the flow field. In particular, the intersection of the plate shock with the jet shock must run

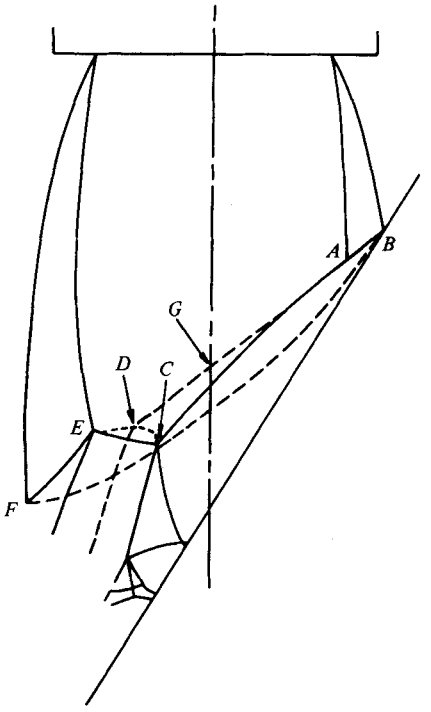

FIGURE 30. Annotated tracing of figure 25(*b*). Letters are referred to in the text.

around the entire circumference of the jet shock. This intersection is visible on figure 25(*b*) and appears as the dashed line *AGDE* on figure 30, which is an annotated tracing of figure 25(*b*). Now, at *E* and *A* the intersection line is perpendicular to the upstream velocity which means that two-dimensional shock confluence theory can be applied (Henderson 1966). Elsewhere, the intersection is inclined to the upstream velocity vector and the flow is three-dimensional. Hunt & Lamont (1978) have analysed this situation and have shown that a three-dimensional triple shock intersection can be transformed into an equivalent planar confluence point. A similar analysis (to be reported) has been performed on the regular crossing point of two shock waves, again an equivalent planar confluence point exists. In the light of this, consider the possibility of a smooth plate shock extending to form a regular crossing point with the lower branch of the jet shock at a hypothetical point *E'*. Now, at *A* there is a triple point and hence there must be some point on the jet shock between *A* and *E'* where a three-dimensional triple point is contiguous with a three-dimensional regular crossing point. Since the plate shock must be continuous through the junction, the direction of the intersection line must locally be the same for both confluences. The three-dimensional theory shows that the strengths of the jet and plate shocks must then be the same for both confluences in the equivalent two-dimensional flows. This is impossible, however, since the equivalent plate shock must be weak for the regular crossing and must be strong at a triple point. It therefore follows that the transition from a three shock confluence in the upper part of the flow field to a regular crossing in the lower part is not possible. An intermediate triple point is created instead.

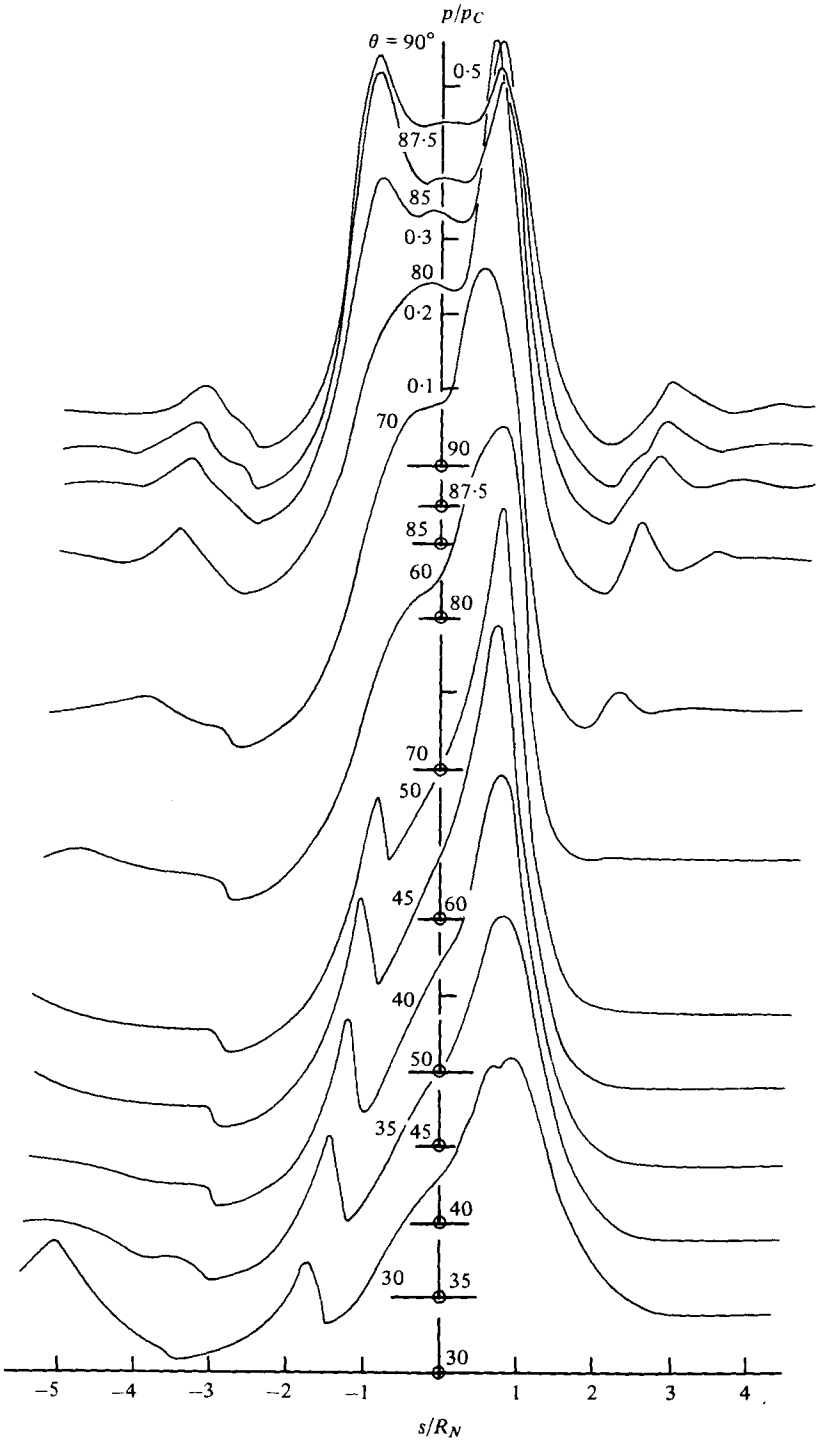

FIGURE 31. Surface pressures on the plane of symmetry for $z_{NP} = 3D_N$ and $PR = 1{\cdot}2$.

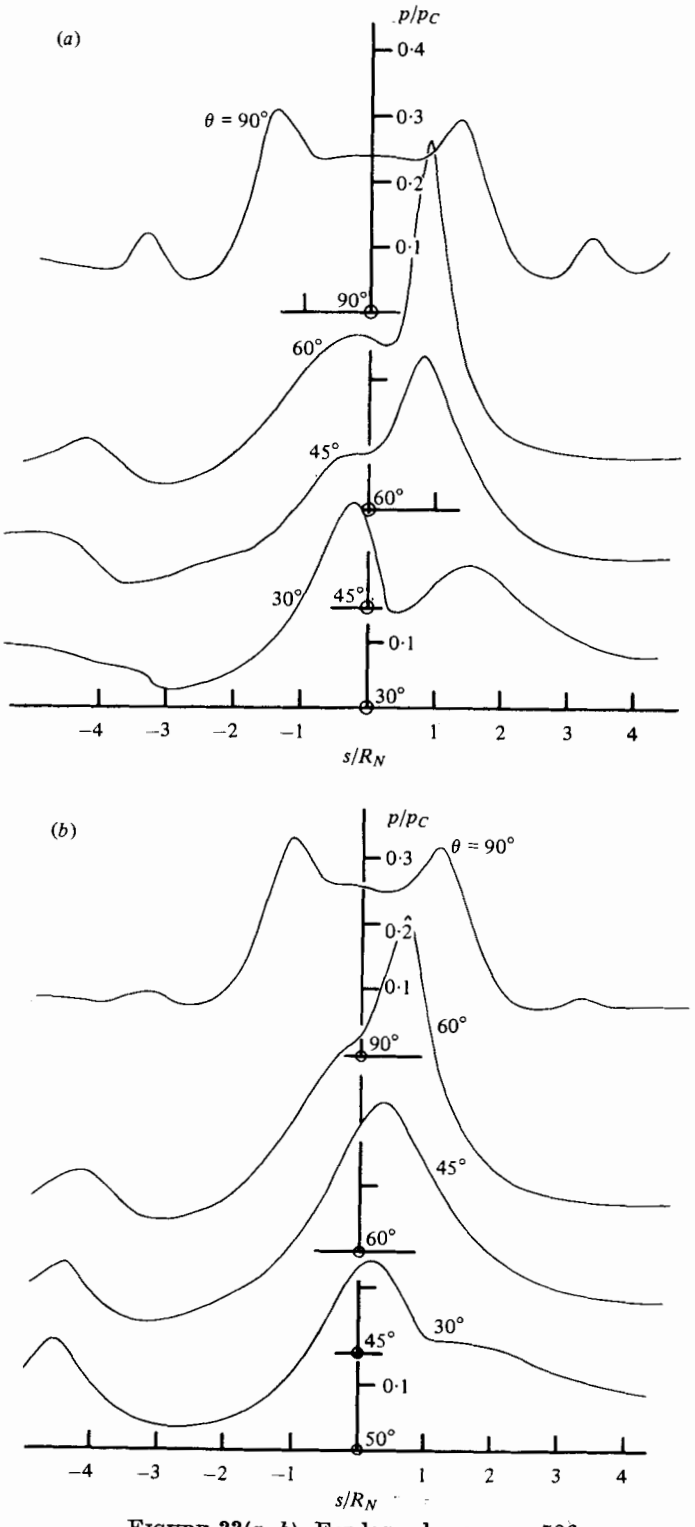

FIGURE 33(*a*, *b*). For legend see page 506.

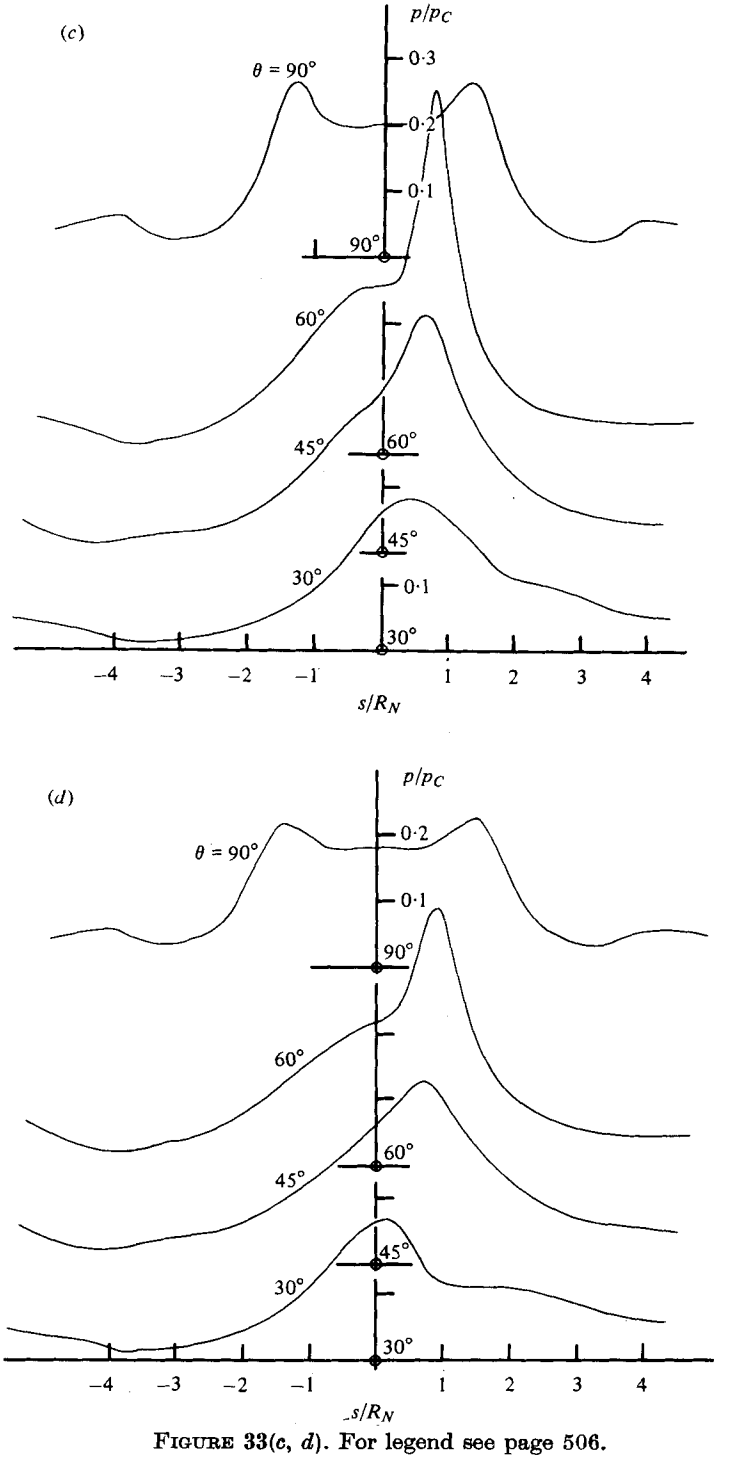

FIGURE 33(c, d). For legend see page 506.

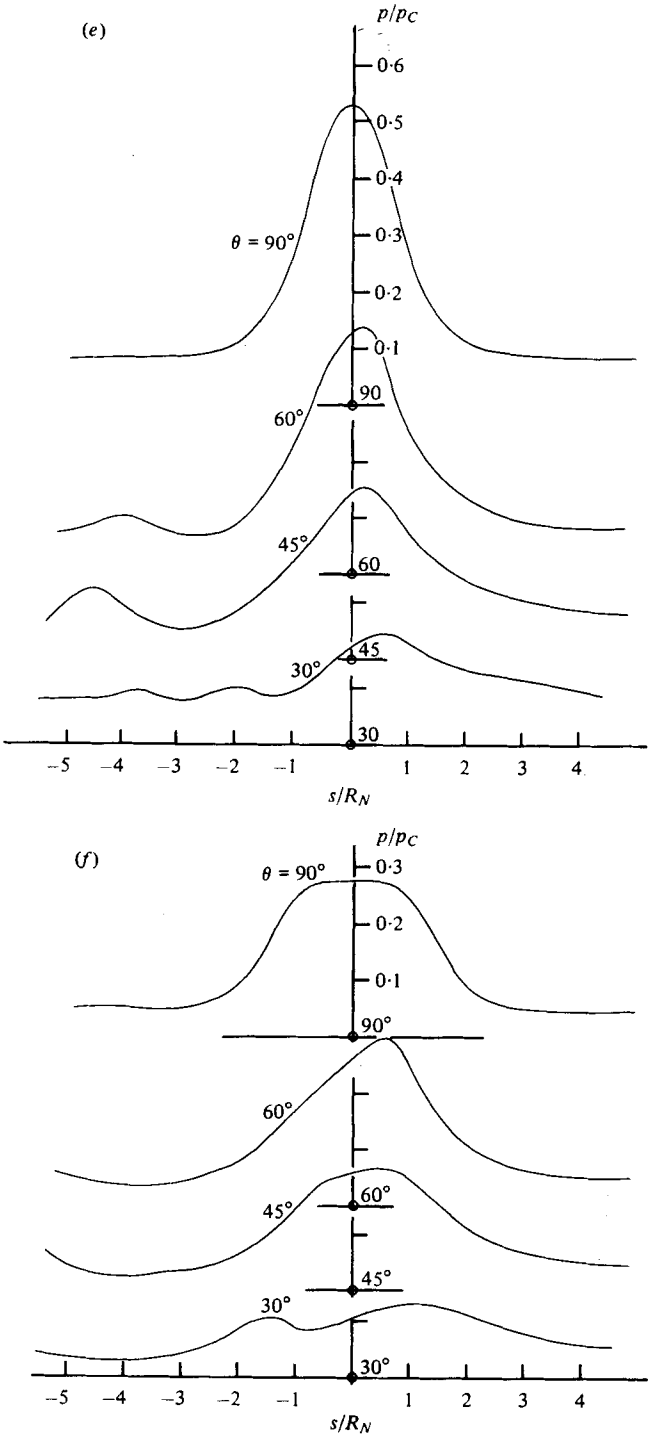

FIGURE 33. Surface pressures on the plane of symmetry at moderate distances from the nozzle. (*a*) $z_{NP} = 7D_N, PR = 1{\cdot}2$; (*b*) $z_{NP} = 7D_N, PR = 2$; (*c*) $z_{NP} = 10D_N, PR = 1{\cdot}2$; (*d*) $z_{NP} = 10D_N$, $PR = 2$; (*e*) $z_{NP} = 15D_N, PR = 1{\cdot}2$; (*f*) $z_{NP} = 15D_N, PR = 2$.

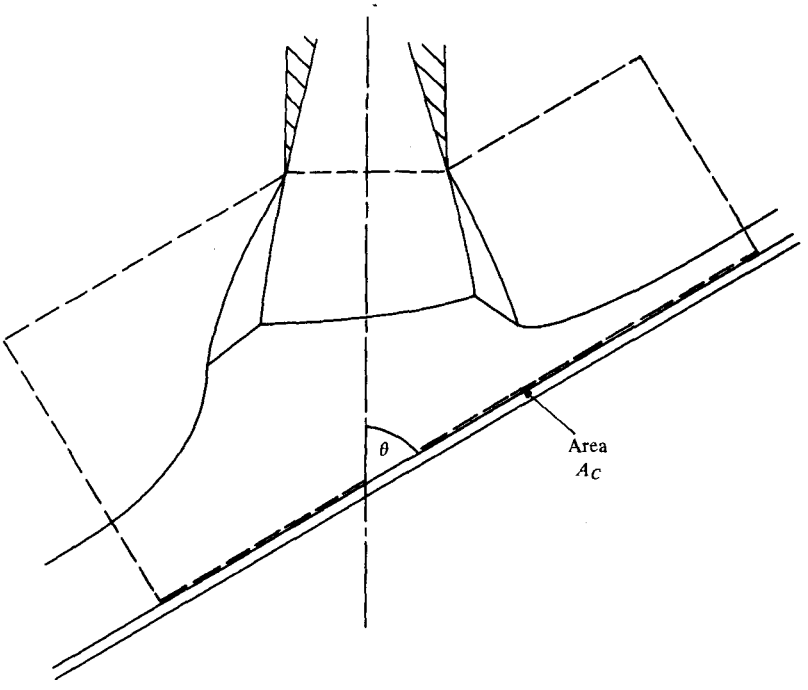

FIGURE 35. Sketch of impingement flow field, showing a control surface.

7.3. *Impingement in the middle and far fields*

The cases discussed in this sub-section are those in which the plate is sufficiently far from the nozzle that at least one shock cell is unaffected by its presence. Detailed analyses of these flows are not possible because the details of the relevant parts of the free jet are not known and because flow features are not well defined in the shadowgraphs because of the effects of turbulence. Nonetheless, some comments can be made.

Figure 31 shows the central-plane pressures for $z_{NP} = 3D_N$, $PR = 1{\cdot}2$. Figure 32 (plate 10) presents a shadowgraph at the plate angle $\theta = 45°$. For $\theta < 45°$, the plate shock is similar to that seen in figure 32 but of course it becomes more symmetrical as θ increases. For $\theta \geqslant 85°$, figure 31 shows that a bubble exists, produced by the shear layer which originates at the edge of the Mach disk. The peak pressures achieved tend to be large: the highest plate pressure recorded anywhere in this study occurs at $\theta = 80°$ where it has the value of $0{\cdot}77p_C$. When θ falls below 45°, the peak values start to reduce: this appears to be due to some structuring of the upper part of the plate shock. A striking feature of the distributions of figure 31 is the sharp rise which occurs when s is negative for $\theta \leqslant 50°$. This is clearly associated with a wave, an example of which can be seen in figure 32. At first sight, this wave appears to be associated with the jet edge: this, however, is not possible since the interaction of a plate shock and a jet edge produces expansion waves (Carling & Hunt 1974). A more likely explanation is that the wave is the tail shock of a three shock confluence point, the bow shock of which is almost lost in the edge shear layer. Some confirmation of this is given by the observation that the measured angle of the lower part of the plate shock corresponds to a weak shock for $\theta \leqslant 50°$ but to a strong shock for $\theta \geqslant 60°$.

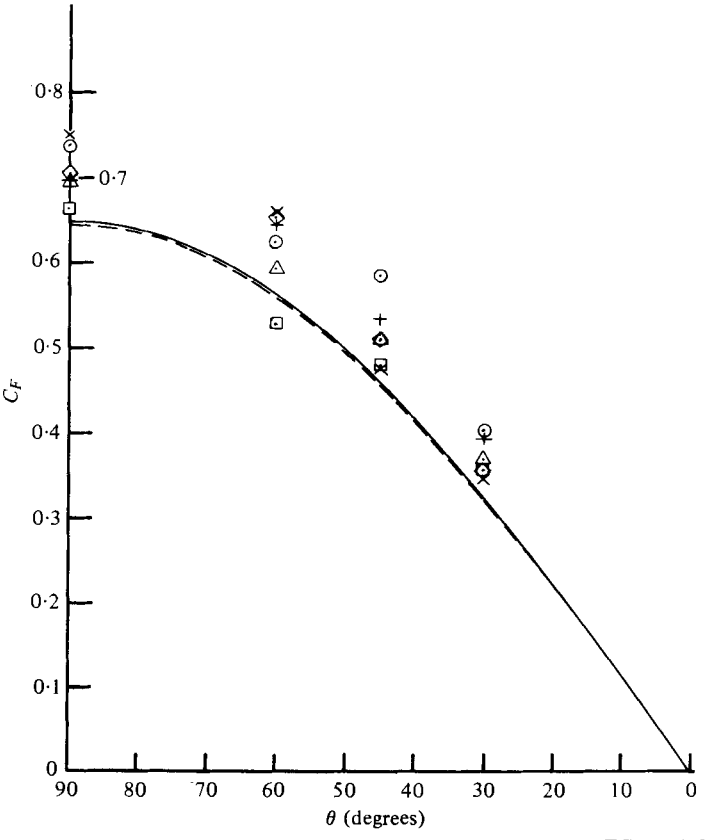

FIGURE 36. Variation of force coefficient with plate inclination for $PR = 1{\cdot}2$. – – –, equation (1) using nozzle exit conditions from the Lockheed plume program; ——, equation (2). Symbols are integrated pressure loads for the following values of z_{NP}/D_N: ⊡, 1; ⊙, 2; △, 3; +, 7; ×, 10; ◇, 15.

Figures 33(*a*)–(*f*) contain the central pressure distributions for $z_{NP} = 7D_N$, $10D_N$ and $15D_N$ at the two pressure ratios. The shadowgraphs at the two smaller plate displacements contain some features but nothing could be seen at $z_{NP} = 15D_N$. Figure 34 (plate 10) shows a shadowgraph obtained at $z_{NP} = 7D_N$, $PR = 1{\cdot}2$ and $\theta = 30°$. The horizontal line is a wire set to mark the plane $z_{NP} = 7D_N$.

For $z_{NP} = 15D_N$ and $PR = 1{\cdot}2$ (figure 32*e*), the free jet is subsonic and the pressure distributions have the smooth forms and general features observed by Donaldson & Snedeker (1971) in those of their tests where the jet was subsonic. In all other cases, the free jets are supersonic and the effects of waves and shear layers can be seen in the rapid pressure changes and sharp peaks. The general trends are the same as those seen in the near field in that the peak pressure initially rises as θ falls and then reduces. In figure 33(*a*), a sharp pressure rise can be seen near the axis for $\theta = 30°$. Figure 34 is the corresponding shadowgraph. The wave responsible for the compression is visible; it seems to be the tail shock from a rather diffuse three shock confluence point.

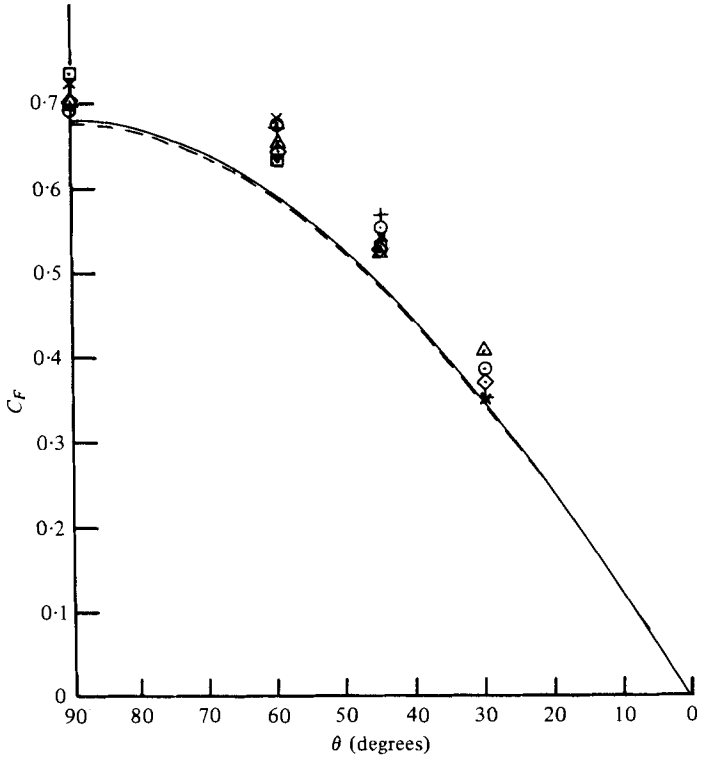

FIGURE 37. Variation of force coefficient with plate inclination for $PR = 2$. Legend as figure 36.

8. Normal forces

The overall load on the plate is a quantity of considerable practical importance. The dominant component of this load is the force normal to the plate produced by the surface pressures. In this section, this normal force is evaluated by consideration of a momentum balance and the predicted values are compared to those obtained by integrating the surface pressures over the complete footprint.

Figure 35 shows the choice of control volume. The flow through the sides is taken to be parallel to the plate and the momentum fluxes and gauge pressure forces due to the entrainment flows through the various surfaces are assumed to be negligible. Since the nozzle is axisymmetric, the exit plane pressure force and momentum flux will be directed along the axis. One finds on resolving perpendicular to the plate that, if F_P is the gauge pressure force on the plate, then the force coefficient, C_F is given by

$$C_F \equiv \frac{F_P}{p_C A_N} = 2\sin\theta \int_0^1 \left(\frac{p}{p_C} - \frac{p_a}{p_C} + \frac{p}{p_C}\gamma M^2 \cos^2\alpha\right) \frac{r}{R_N} d\left(\frac{r}{R_N}\right), \tag{1}$$

where A_N is the exit area of the nozzle, the integration takes place in the nozzle exit plane and α is the local inclination of the flow to the centre-line.

For the present problem, (1) has been evaluated numerically for the exit-plane conditions given by the Lockheed plume program. It can be evaluated more easily if radial flow is assumed at the nozzle exit. The control surface across the nozzle exit

is then conveniently replaced by a spherical gap along which the Mach number is constant at the lip value of M_N. Equation (1) can then be expressed as

$$C_F = \sin\theta \frac{p_N}{p_C}\left(1 - \frac{p_a}{p_N} + \gamma M_N^2\right). \tag{2}$$

Figures 36 and 37 present measured and predicted values of C_F as a function of θ for the two pressure ratios, $PR = 1{\cdot}2$ and $PR = 2$ respectively. It can be seen by comparing the two figures that C_F is insensitive to the pressure ratio, as is implied by (2), where p_N/p_C is a function of M_N but not of $PR \equiv p_N/p_a$. The difference between using conditions from the Lockheed plume program and assuming radial flow is seen to be very small. The experimental results exhibit a scattered variation with plate location, z_{NP}. A likely explanation for this is that the integration of measured pressures is not a particularly accurate means of obtaining overall loads since small errors in the measurement of wall jet pressures act on a large area and hence produce significant errors in the overall load. The scatter on the figures corresponds to an error of $\pm$ 1400 N m^{-2}; this is considerably less than the nominal nonlinearity and hysteresis of the transducer which are approximately 8500 N m^{-2}.

Figures 36 and 37 also show that the values of measured loads tend to be higher than those predicted. This may also be due to small errors in the measured pressures but a bias in the errors is then implied. This is by no means impossible. A second possible source of discrepancy lies in the neglect of momentum flux and static pressure due to entrainment. The integrated pressure loads obtained for $\theta = 90°$ by Snedeker & Donaldson (1964) were found to be substantially greater than the momentum at nozzle exit and this was ascribed to the influence of entrainment. However, if entrainment were the cause in the present study, the experimental load would be expected to show a smooth variation with z_{NP} rather than the scatter which is to be seen in figures 35 and 36. Even for the impingement of subsonic jets, the relation between measured force and exit jet momentum does not seem to have been fully investigated and further work on this point would be justified.

9. Conclusions

An extensive study of the flows due to supersonic jets impinging on flat plates has been conducted.

The local structure of the jet has been found to have a strong influence on the flow fields. In particular, the interactions between shock waves in the free jet and those created by the plate have very strong influences on the pressures found on the plate. In the near field, these wave interactions tend to be the controlling factors but at larger distances from the nozzle, mixing effects become increasingly important.

One of the consequences of the creation of multiple shock waves in the flow is that the peak pressures on an inclined plate can exceed those on a perpendicular plate by very large amounts – up to a factor of 3 in the cases tested. This behaviour is in strong contrast to that which occurs in the far field, where the maximum pressure is always reduced by inclining the plate.

It has been found possible in the near field to reconstruct the shock patterns and many features of the central plane pressure distributions on the basis of an inviscid model of the free jet. However, the existence of an edge shear layer is important in

some circumstances: there are situations in which the edge shear layer allows the leading section of plate shock to behave as though it is attached when inviscid theory would require a detached shock. Three-dimensional effects have been shown to be important in creating one of the more common features of the shock patterns, the intermediate triple point.

For the particular case of a perpendicular plate, some success has been demonstrated in the correlation of pressures, shock location and the occurrence of stagnation bubbles.

The overall integrated pressure loads were found to be predicted reasonably well by a simple momentum balance.

This work has been carried out with the support of the Procurement Executive, Ministry of Defence. The interest and encouragement of Mr D. Cairns (British Aerospace), Mr S. W. H. Perry (Ministry of Defence) and Mr A. Wilson (Propulsion, Explosives and Rocket Motor Establishment) are gratefully acknowledged. Particular thanks are due to Mr Wilson for providing the solutions from the Lockheed plume program.

REFERENCES

BACK, L. H. & CUFFEL, R. F. 1966 *A.I.A.A. J.* **4**, 2219.

BACK, L. H. & SAROHIA, V. 1978 *A.I.A.A. J.* **16**, 634.

BUTLER, H. W. 1966 *N.A.S.A. Contractors Rep.* CR-81143.

CARLING, J. C. & HUNT, B. L. 1974 *J. Fluid Mech.* **66**, 159.

CLARK, L. V. 1970 *N.A.S.A. Tech. Note* D-5895.

DONALDSON, C. DUP. & SNEDEKER, R. S. 1971 *J. Fluid Mech.* **45**, 281.

EDNEY, B. 1968 *Aero. Res. Inst. Sweden FFA Rep.* no. 115.

GINZBURG, I. P., BELOV, I. A., ZAZIMKO, V. A. & TERPIGOR'EV, V. S. 1968 *Heat & Mass Transfer (Minsk)* **1**, 381.

GINZBURG, I. P., SEMILETENKO, B. G., TERPIGOR'EV, V. S. & USKOV, V. N. 1970 *J. Engng Phys. U.S.S.R.* **19**, 412.

GUBANOVA, O. I., LUNEV, V. V. & PLASTININA, L. I. 1974 *Fluid Dyn.* **6**, 135.

GUMMER, J. H. & HUNT, B. L. 1971 *Aero. Quart.* **22**, 403.

GUMMER, J. H. & HUNT, B. L. 1974 *Israel J. Tech.* **12**, 221.

HENDERSON, L. F. 1964 *Aero. Quart.* **15**, 181.

HENDERSON, L. F. 1966 *Z. angew. Math. Phys.* **17**, 553.

HUNT, B. L. & LAMONT, P. J. 1978 *Aero. Quart.* **29**, 18.

KALGHATGI, G. T. & HUNT, B. L. 1976 *Aero. Quart.* **27**, 169.

LAMONT, P. J. & HUNT, B. L. 1976 *J. Fluid Mech.* **76**, 307.

LAMONT, P. J. & HUNT, B. L. 1977 *University of Bristol, Aero. Dept. Rep.* PJL/7701, BLH/7703 (2 vols).

NAKATOGAWA, T., HIRAT, M. & KUKITA, Y. 1971 *J. Spacecraft* **8**, 410.

PROZAN, R. J. 1966 *Lockheed Missiles and Space Company Rep.* LMSC/HREC A78235-A.

SAUER, R. 1947 *N.A.C.A. Tech. Memo.* 1047.

SEMILETENKO, B. G. & USKOV, V. N. 1972 *J. Engng Phys. U.S.S.R.* **23**, 453.

SNEDEKER, R. S. & DONALDSON, C. DUP. 1964 *Aero. Res. Ass. Princeton Rep.* no. 63.

SNEDEKER, R. S. & DONALDSON, C. DUP. 1965 *Aero. Res. Ass. Princeton Rep.* no. 64.

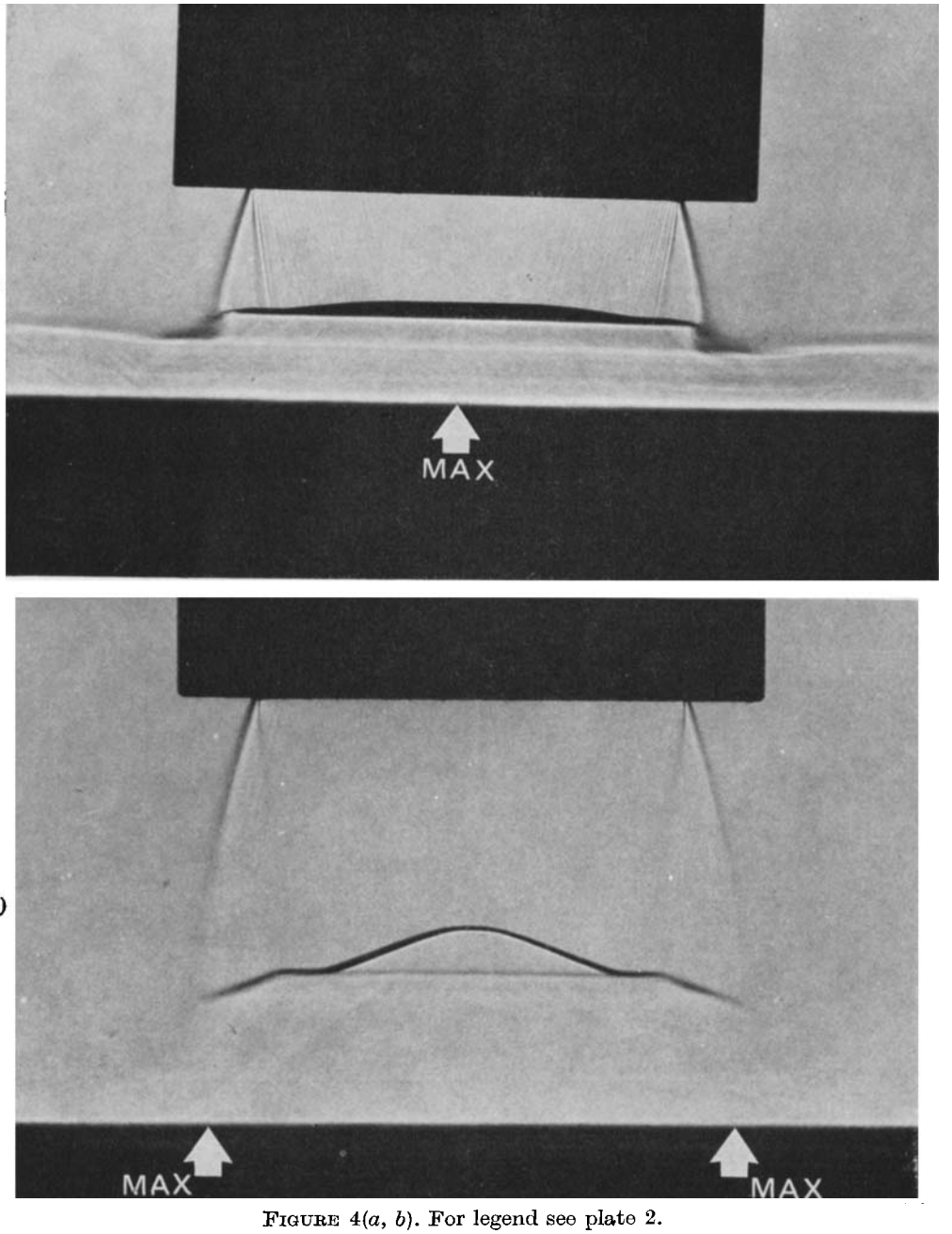

FIGURE 4(*a*, *b*). For legend see plate 2.

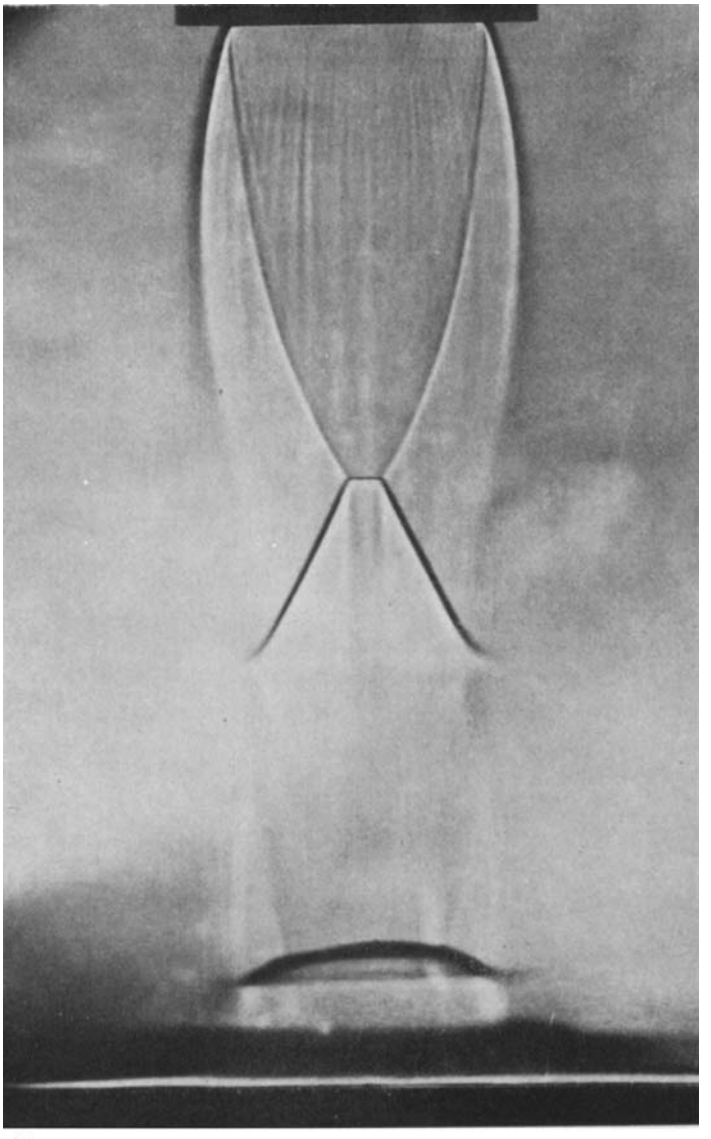

(*c*)

FIGURE 4. Shadowgraphs for the plate perpendicular to the jet axis ($\theta = 90°$).
(*a*) $z_{NP} = 0{\cdot}5D_N$, $PR = 1{\cdot}2$; (*b*) $z_{NP} = D_N$, $PR = 1{\cdot}2$; (*c*) $z_{NP} = 4D_N$, $PR = 1{\cdot}2$.

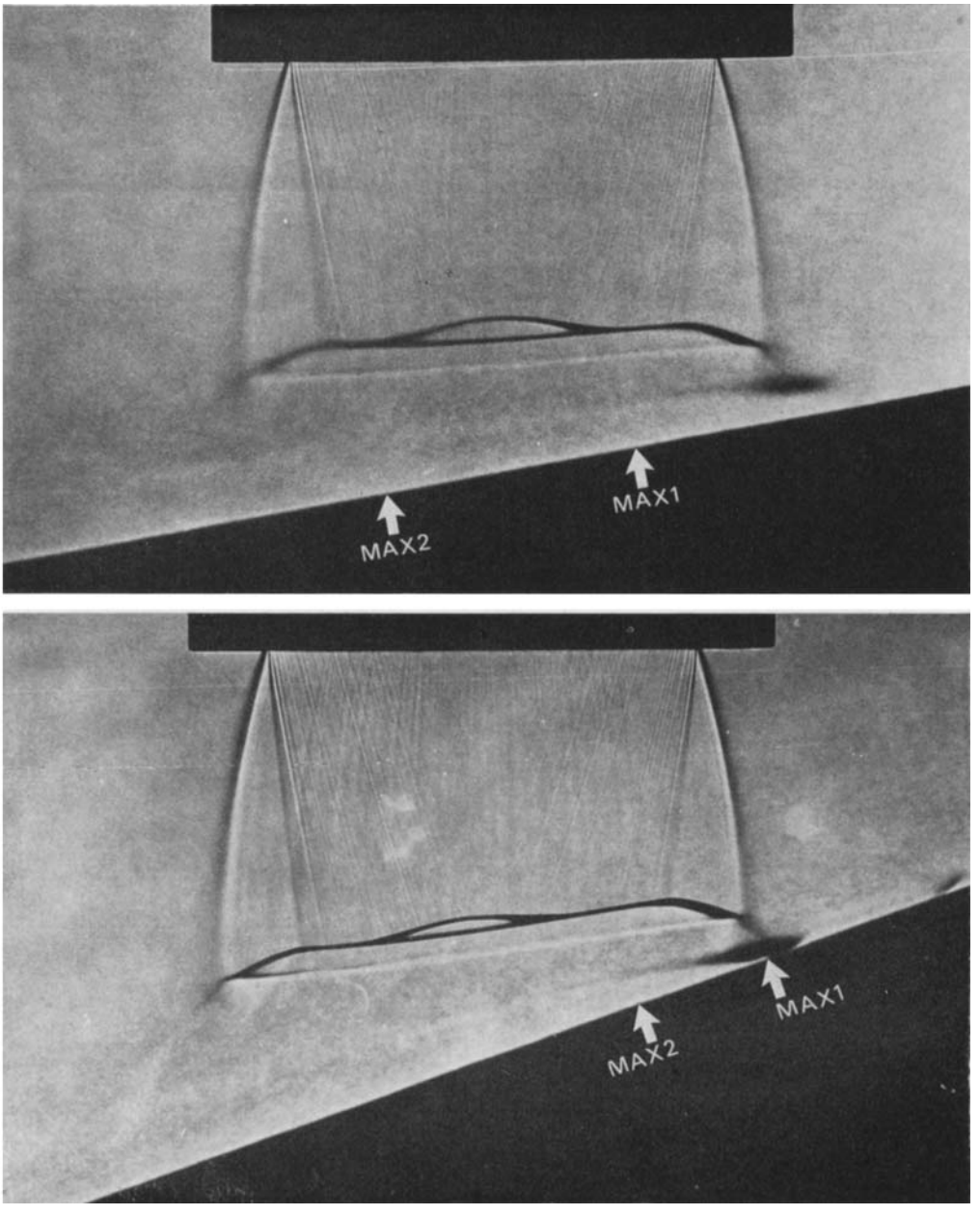

FIGURE 12(*a*, *b*). For legend see plate 4.

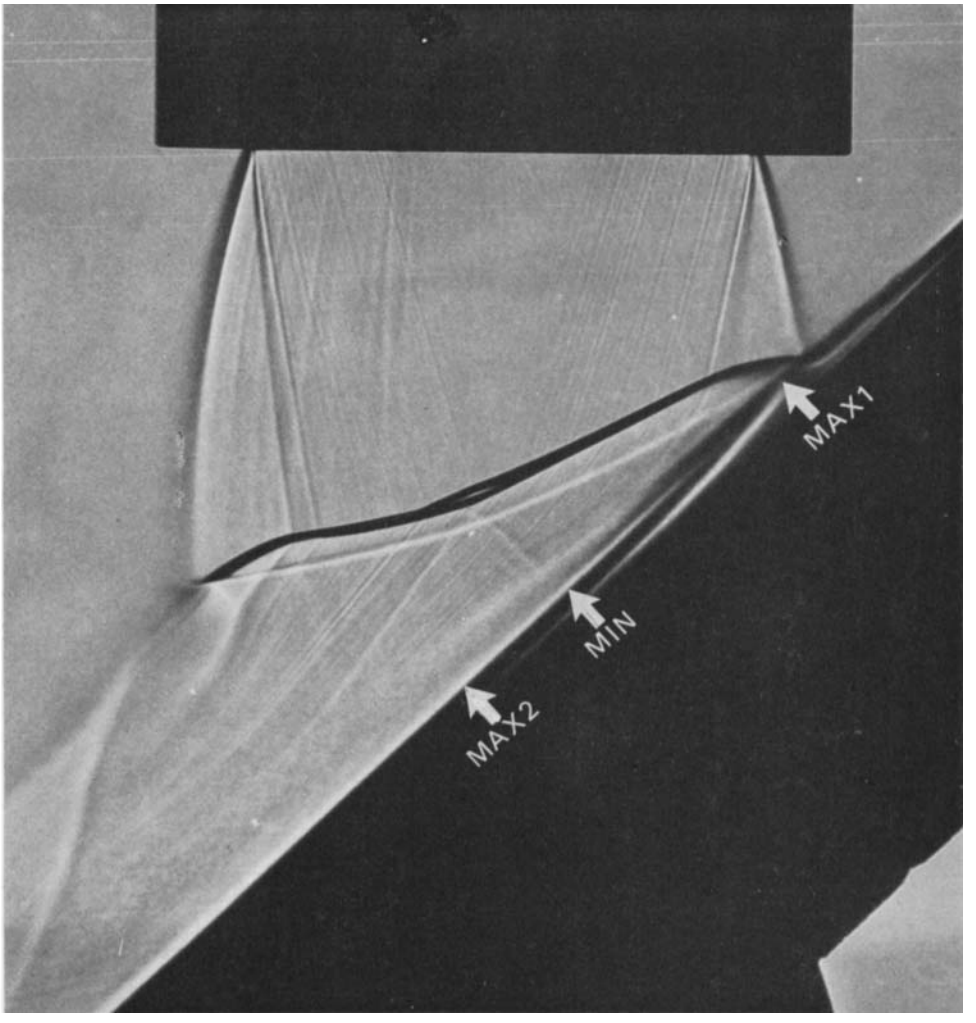

FIGURE 12. Shadowgraphs for $z_{NP} = D_N$ and $PR = 1{\cdot}2$.
(*a*) $\theta = 80°$, (*b*) $\theta = 70°$, (*c*) $\theta = 45°$.

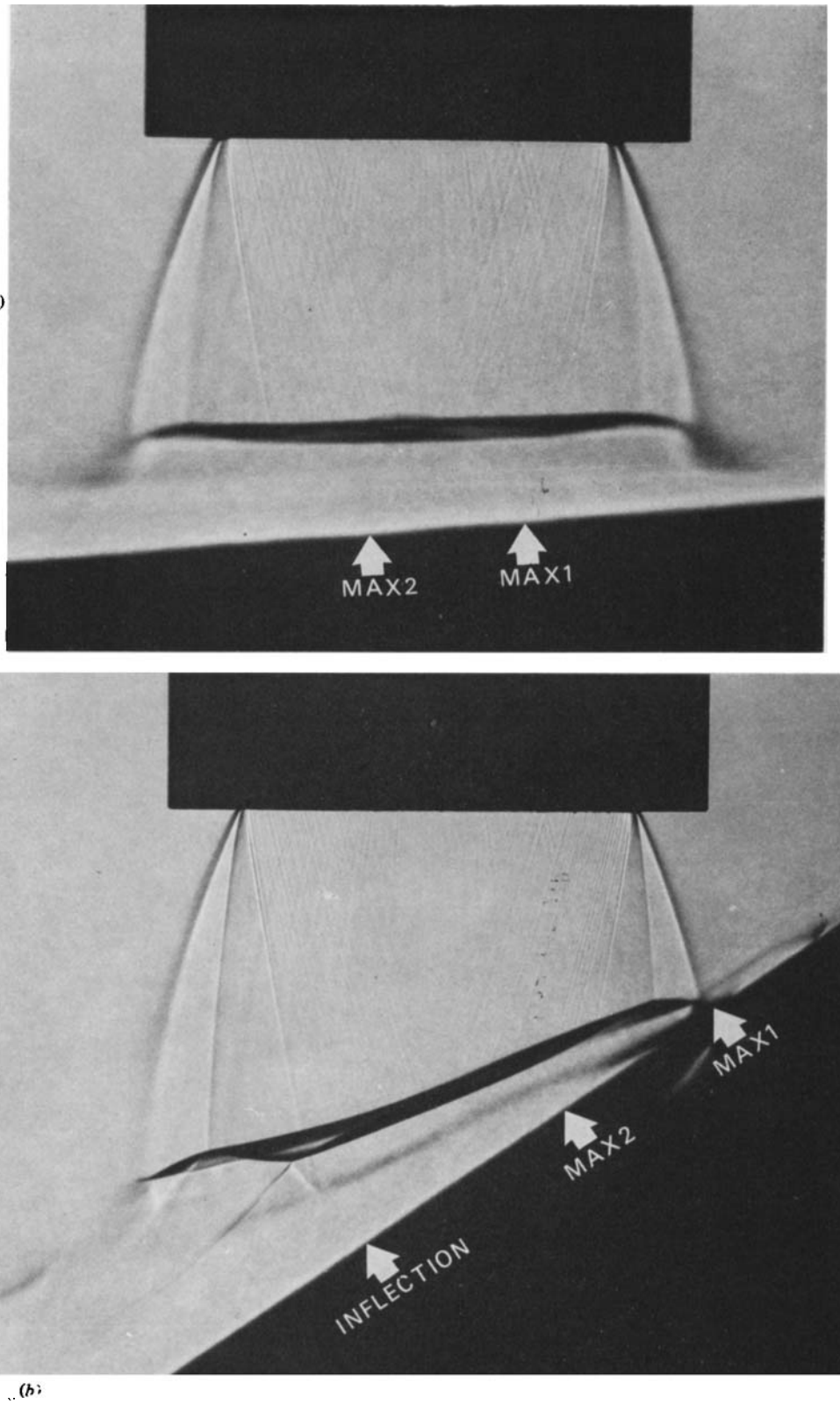

FIGURE 15(*a*, *b*). For legend see plate 6.

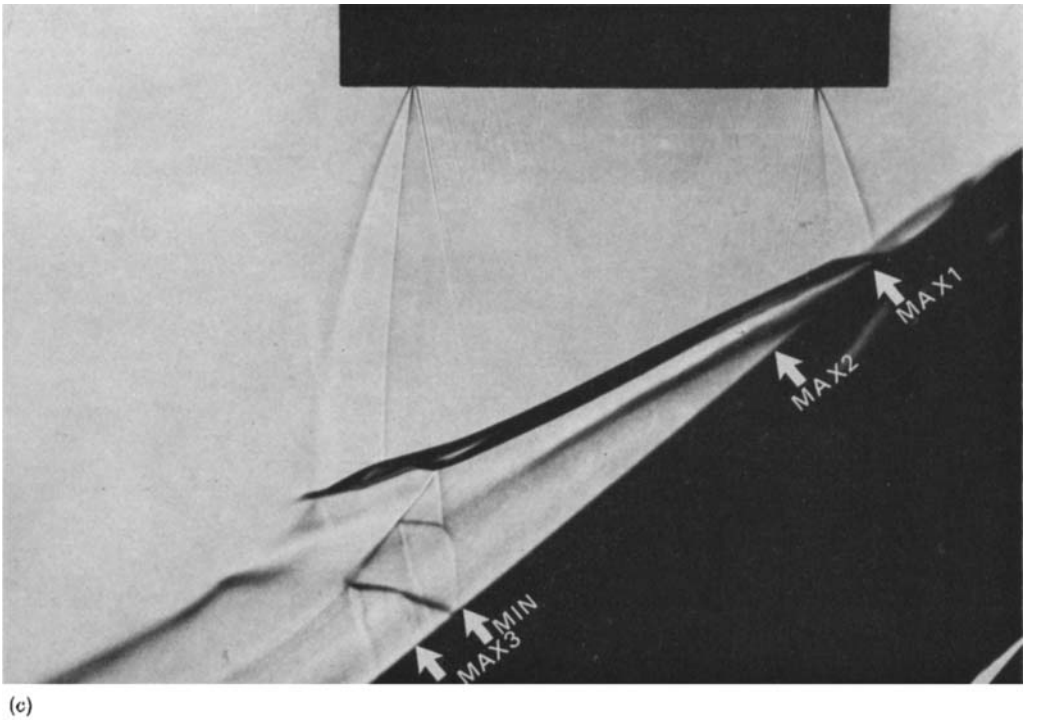

(c)

FIGURE 15. Shadowgraphs for $z_{NP} = D_N$ and $PR = 2$.
(*a*) $\theta = 85°$, (*b*) $\theta = 55°$, (*c*) $\theta = 50°$.

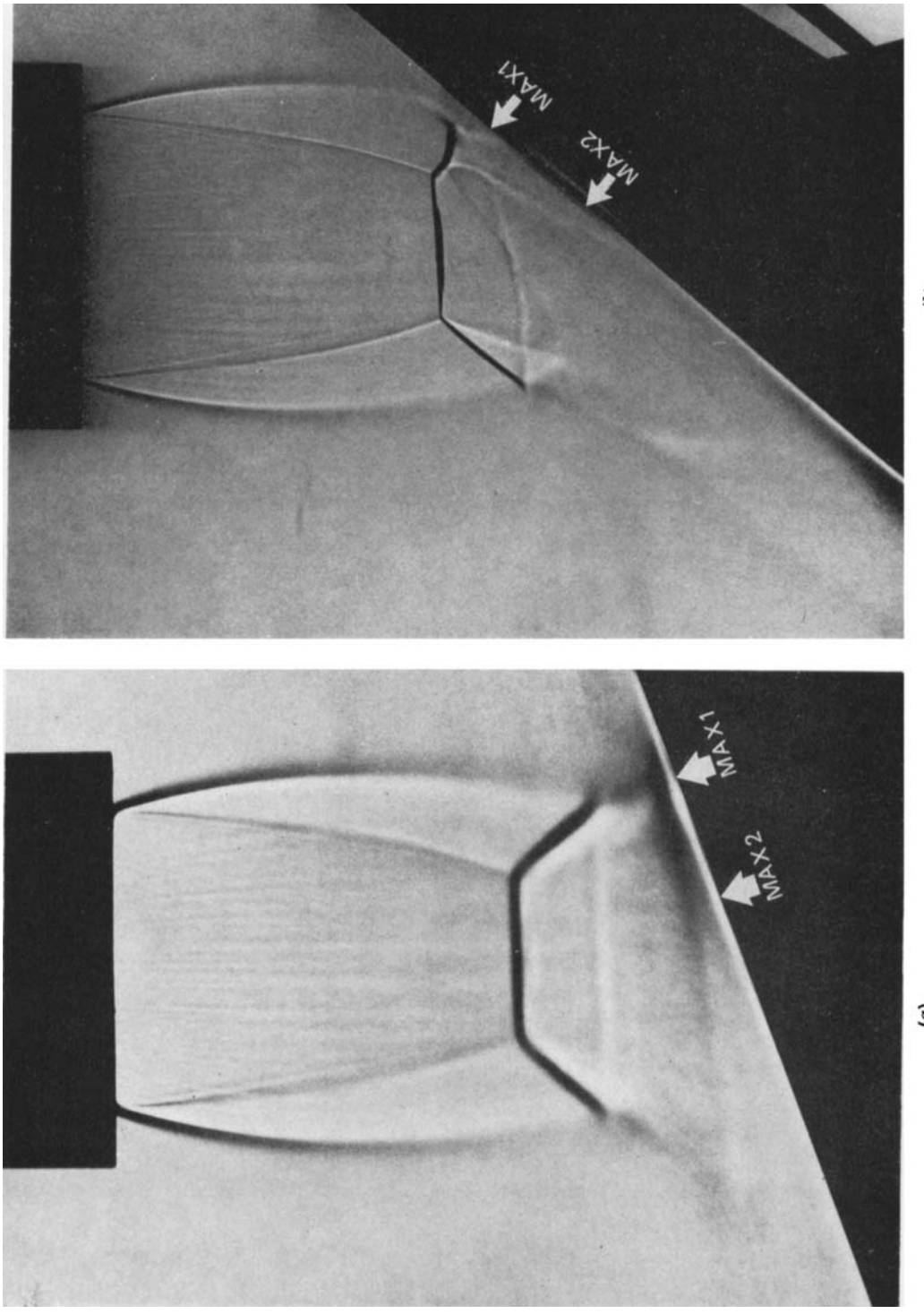

FIGURE 18 (*a*, *b*). For legend see plate 8.

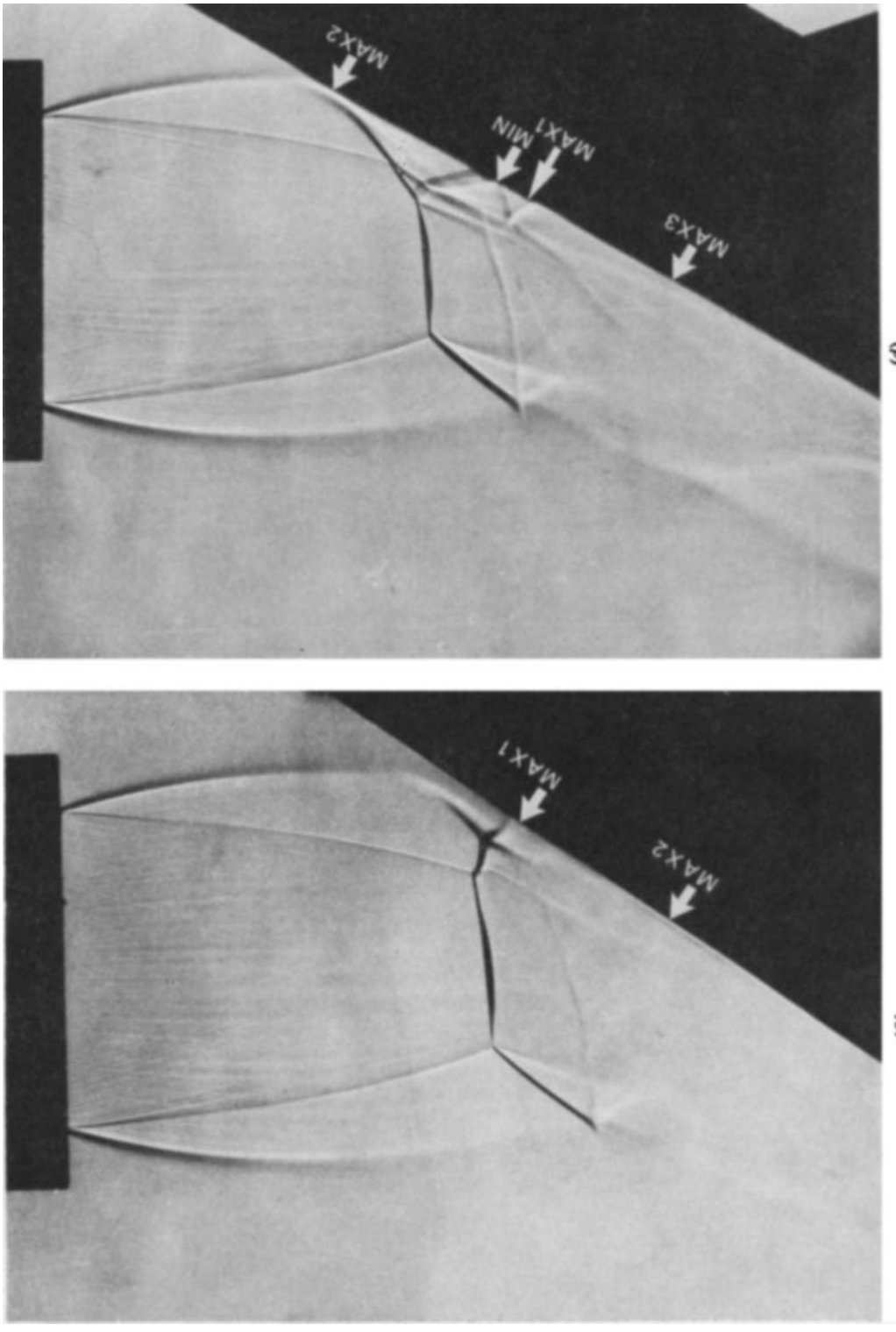

FIGURE 18. Shadowgraphs for $z_{NP} = 2D_N$ and $PR = 1{\cdot}2$.
(*a*) $\theta = 70°$, (*b*) $\theta = 40°$, (*c*) $\theta = 35°$, (*d*) $\theta = 30°$.

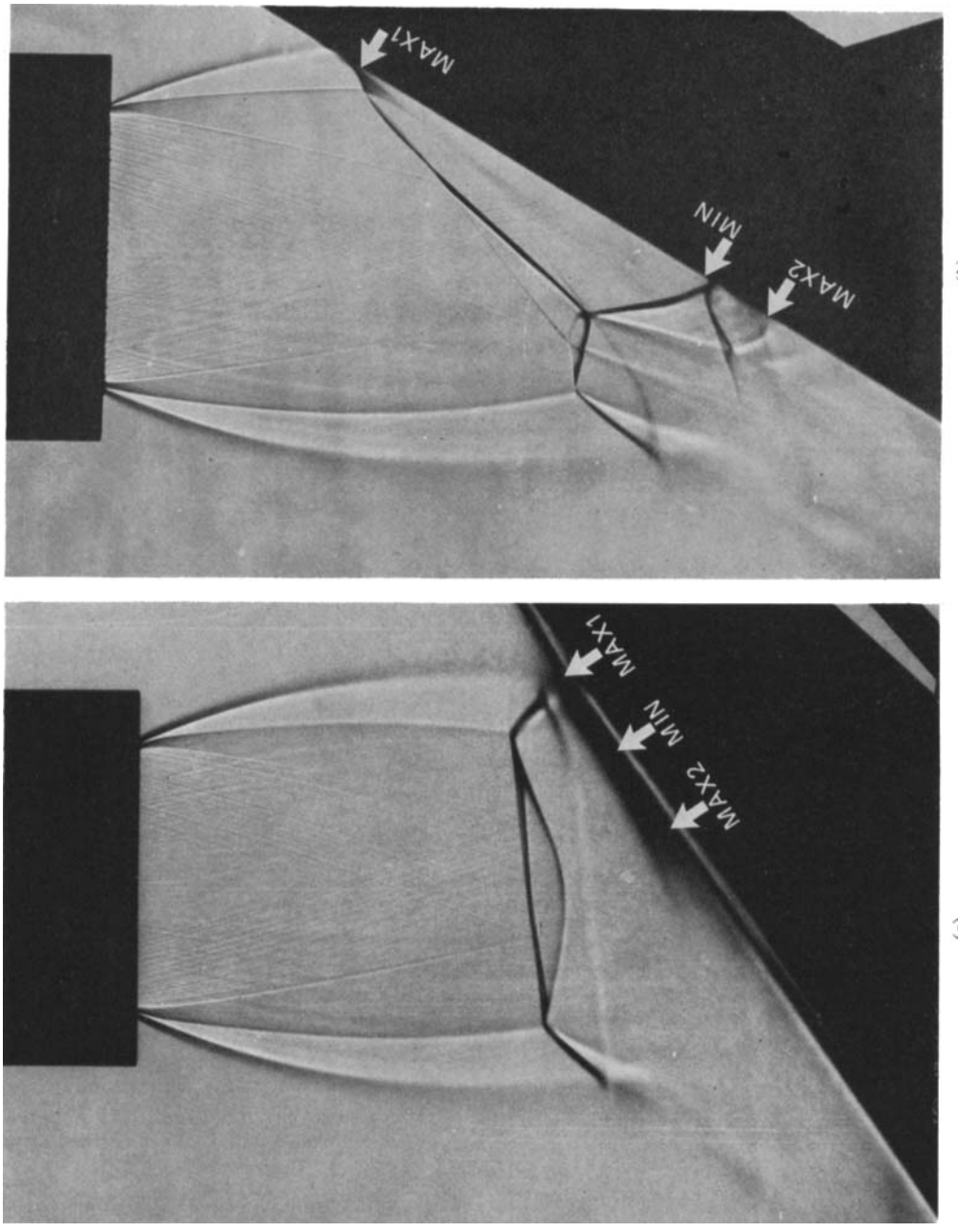

FIGURE 25. Shadowgraphs for $z_{NP} = 2D_N$ and $PR = 2$. (*a*) $\theta = 55°$, (*b*) $\theta = 30°$.

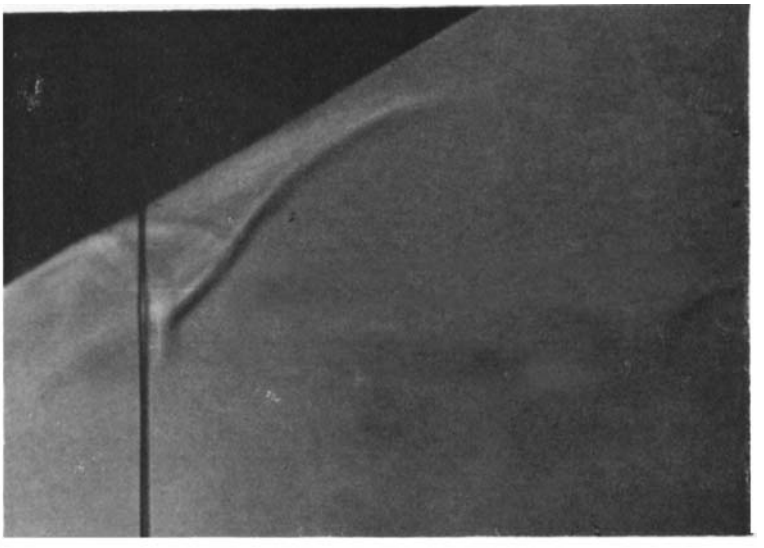

FIGURE 34. Shadowgraph for $z_{NP} = 7D_N$, $PR = 1{\cdot}2$ and $\theta = 30°$.

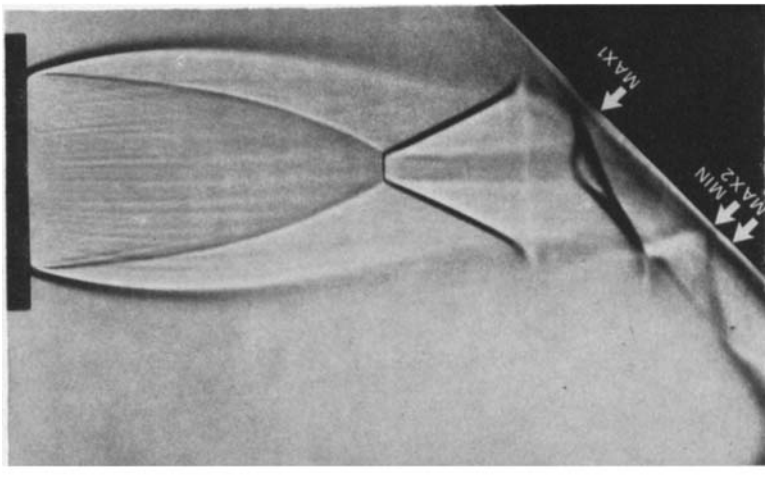

FIGURE 32. Shadowgraph for $z_{NP} = 3D_N$, $PR = 1{\cdot}2$ and $\theta = 45°$.

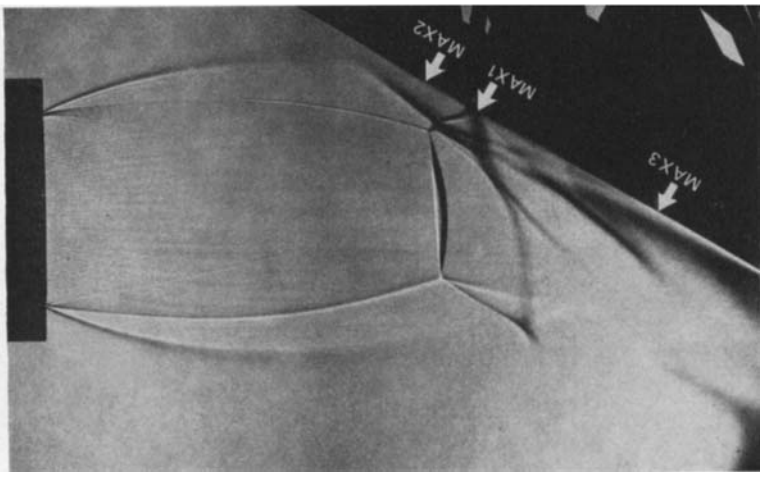

FIGURE 29. Shadowgraph for $z_{NP} = 3D_N$, $PR = 2$ and $\theta = 30°$.